Journal of Computational Physics 418, 109636
https://doi.org/10.1016/j.jcp.2020.109636

A level-set method for moving contact lines with contact angle hysteresis

Jiaqi Zhang[a], Pengtao Yue[a]

[a]*Department of Mathematics, Virginia Tech, Blacksburg, VA 24061, USA*

Abstract

We develop a level-set method in the finite-element framework. The contact line singularity is removed by the slip boundary condition proposed by Ren and E [Phys. Fluids 19 (2007) 022101], which has two friction coefficients: β_N that controls the slip between the bulk fluids and the solid wall and β_{CL} that controls the deviation of the microscopic dynamic contact angle from the static one. The predicted contact line dynamics from our method matches the Cox theory very well. We further find that the same slip length in the Cox theory can be reproduced by different combinations of (β_N, β_{CL}), based on which we come up with a computational strategy for mesh-independent results that can match the experiments. There is no need to impose the contact angle condition geometrically, and the dynamic contact angle automatically emerges as part of the numerical solution. With a little modification, our method can also be used to compute contact angle hysteresis, where the tendency of contact line motion is readily available from the level-set function. Different test cases, including code validation and mesh-convergence study, are provided to demonstrate the efficiency and capability of our method.

Keywords: contact angle hysteresis, contact line pinning, slip length, drop spreading, GNBC, contact line friction

1. Introduction

The moving contact line problem has attracted intensive research in the past few decades due to its importance in many natural processes and industrial applications. This problem is difficult due to the stress singularity at the

Email addresses: zjiaqi@vt.edu (Jiaqi Zhang), ptyue@vt.edu (Pengtao Yue)

contact line caused by the discrepancy between the no-slip boundary condition and the moving interface. In continuum numerical simulations, different models have been adopted to relax the stress singularity, e.g., Navier slip [1], diffusion (such as those in the Cahn-Hilliard model [2], conservative level set method [3], and lattice Boltzmann method [4]), and the generalized Navier slip [5, 6]. The readers are referred to [7] for a comprehensive review on this topic and we will focus on the generalized Navier slip in this work.

From molecular dynamics (MD) simulations, Qian *et al.* found that the slip velocity at the wall was proportional to the sum of the tangential viscous stress and the uncompensated Young's stress (a.k.a. the unbalanced Young's stress), based on which they developed the generalized Navier boundary condition (GNBC) in the phase-field framework [5]. The velocity profiles in the vicinity of the contact line from their phase-field simulations agreed very well with the MD results. Ren and E later developed a similar slip condition [6], which is no longer restricted to the phase-field method. Their continuum modeling based on the immersed boundary method compared favorably with the MD results. Theoretically, these two slip conditions can also be derived from Onsager's minimum energy dissipation rate principle [8] or simply from the second law of thermodynamics [9]. It should be noted that Ren and E's slip condition is different from the sharp-interface limit of Qian *et al.* 's GNBC [10]. We follow Ren and E's slip condition in this work.

With the support from MD simulations and thermodynamic principles, the generalized Navier slip condition has gained popularity in recent years. In the phase-field community, the GNBC has been frequently adopted for contact line problems, e.g., [11, 12, 13, 14, 15]. Meanwhile, the GNBC has also been adopted in many other numerical methods for interfacial flows. For example, Gerbeau and Lelièvre incorporated the GNBC into a variational arbitrary Lagrangian-Eulerian (ALE) formulation which is well suited for energy stability analysis [16]. Li *et al.* developed an efficient augmented immersed interface method to implement Ren and E's slip condition [17]. Ren and E applied their slip condition to the level-set method and investigated contact line dynamics on heterogeneous surfaces [18]. This level-set work was later extended to moving contact lines with insoluble surfactants [19]. Recently, Zhang and Ren also investigated the influence of viscoelasticity on contact line dynamics using an immersed boundary method combined with the generalized slip condition [20]. The implementation of the GNBC in the front-tracking method can be found in [21]. Most recently, the GNBC was also extended to the volume-of-fluid method [22, 23].

Although the generalized Navier slip has been widely used, it is still challenging to obtain mesh-independent results, because the physical slip

length is usually at the nanoscale and can not be resolved by the computational mesh. It has been shown that Ren and E's slip condition cannot remove the weak singularity at the contact line [24, 25]. Furthermore, Ren and E's slip condition introduces two friction coefficients (β_{CL} and β_N in Section 2.1) rather than a single slip length, and it is unclear how to choose them for predictive simulations that can match the experiments. In this work, we aim to address these issues based on a level-set method. In the literature, a standard treatment to remove mesh dependency, as proposed in [26, 27, 28, 29], is to determine a numerical contact angle at the grid scale based on mascroscale models such as the Cox-Voinov model [30, 31]; this numerical angle is then applied at the contact line in place of the static contact angle. A drawback of this method is that it requires the input of contact line velocity, which may be difficult to obtain, especially in three dimensions. The similar idea was also used in the GNBC, however, in a different flavor [21, 32]: the grid-scale contact angle from the simulation is used to determine a microscopic dynamic contact angle, which is then fed to the GNBC to compute the slip velocity. In this work, we propose a different approach which does not rely on hydrodynamic models and is thus much easier to implement. Meanwhile, by properly choosing the friction coefficients, we will show that Ren and E's slip condition itself is sufficient to reproduce the well-established Cox theory [31] with realistic slip lengths.

Another challenging issue is the contact angle hysteresis, since most solid surfaces are intrinsically rough or chemically heterogenous. In this case, the contact line stays pinned when the microscopic dynamic contact angle is between a receding contact angle θ_R and an advancing contact angle θ_A. The most popular approach for contact angle hysteresis was developed by Spelt for a level-set method [33]. An intermediate contact angle is obtained such that the contact line is pinned. If this angle is within the hysteresis window, the solution is accepted; otherwise, the solution is abandoned and the contact line is moved with prescribed contact angles. This idea was later extended to different methods, eg., the phase-field method [34], the volume-of-fluid method [35], the Lattice Boltzmann method [36], and the front-tracking method [37]. However, this approach relies on ghost cells outside the boundary to pin the contact line or to impose the contact angle condition, which can be challenging on curved boundaries and unstructured meshes. Recently, we developed a thermodynamically consistent phase-field model for contact angle hysteresis [38]. Since the dynamic contact angle is part of the solution instead of being imposed, this method is easy to implement and automatically captures the pinning, advancing, and receding of the contact line. Motivated by [38], we will show that Ren and E's slip

condition can also be easily modified to capture the contact angle hysteresis.

The rest of this paper is organized as follows. We first introduce the governing equations and numerical methods in Section 2. We then explain how to incorporate contact angle hysteresis in Section 3. The numerical results, including code validation and mesh convergence studies, are given in Section 4.

2. Level-set method for moving contact line problems

2.1. Governing equations

Consider an incompressible system of two immiscible Newtonian fluids on an impermeable solid surface, as shown in Fig. 1. We use the level-set method [39, 40] to track the interface implicitly. The interface is represented by the zero level set of a signed distance function ϕ that is evolved by the level-set equation

$$\frac{\partial \phi}{\partial t} + \mathbf{u} \cdot \nabla \phi = 0. \tag{1}$$

The regions with $\phi > 0$ and $\phi < 0$ are occupied by fluid 1 and fluid 2, respectively.

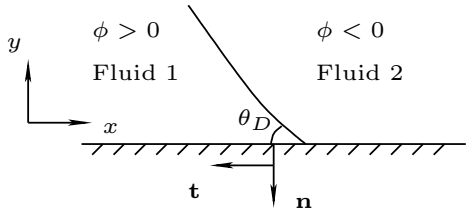

Figure 1: Schematic of a moving contact line on a solid substrate. The (microscopic) dynamic contact angle θ_D is defined with respect to fluid 1, which occupies the region with $\phi > 0$.

Following the level-set literature, the two-phase system can be treated as a single fluid with density and viscosity given by

$$\rho(\phi) = H_\epsilon(\phi)\rho_1 + (1 - H_\epsilon(\phi))\rho_2 \tag{2}$$

and

$$\mu(\phi) = H_\epsilon(\phi)\mu_1 + (1 - H_\epsilon(\phi))\mu_2, \tag{3}$$

where

$$H_\epsilon(\phi) = \begin{cases} 0, & \text{if } \phi < -\epsilon, \\ 1, & \text{if } \phi > \epsilon, \\ \frac{1}{2}\left(1 + \frac{\phi}{\epsilon} + \frac{1}{\pi}\sin\left(\frac{\pi\phi}{\epsilon}\right)\right), & \text{otherwise} \end{cases} \tag{4}$$

is a smooth Heaviside function, 2ϵ is the interface thickness, and the subscripts $_1$ and $_2$ denote fluid 1 and 2, respectively.

For the surface tension term, we adopt the tensor form [41]

$$\boldsymbol{\tau}_\phi = \sigma\delta_\epsilon(\phi)|\nabla\phi|\mathbf{T}(\mathbf{n}_\phi), \tag{5}$$

where σ is the surface tension, $\delta_\epsilon(\phi) = H'_\epsilon(\phi)$ is the smooth Dirac delta function, $\mathbf{n}_\phi = \frac{\nabla\phi}{|\nabla\phi|}$ is the unit normal to the interface, and $T(\mathbf{n}_\phi) = \mathbf{I} - \mathbf{n}_\phi \otimes \mathbf{n}_\phi$. It should be noted that a term $|\nabla\phi|$ is included in (5) to deal with the case where ϕ deviates from a singed distance function.

The incompressible two-phase flow is governed by the momentum equation

$$\rho\left(\frac{\partial\mathbf{u}}{\partial t} + \mathbf{u}\cdot\nabla\mathbf{u}\right) = \nabla\cdot(-p\mathbf{I} + \boldsymbol{\tau} + \boldsymbol{\tau}_\phi) + \rho\mathbf{g} \tag{6}$$

and the continuity equation

$$\nabla\cdot\mathbf{u} = 0, \tag{7}$$

where $\mathbf{u}$ is the fluid velocity, p is the pressure, $\boldsymbol{\tau} = \mu[\nabla\mathbf{u} + (\nabla\mathbf{u})^T]$ is the viscous stress, and $\mathbf{g}$ is the gravitational acceleration.

On the solid wall, we impose the no-penetration condition

$$\mathbf{n}\cdot(\mathbf{u} - \mathbf{u}_w) = 0 \tag{8}$$

in the normal direction and the slip condition in the tangential direction, where $\mathbf{u}_w$ denotes the wall velocity and $\mathbf{n}$ is the outward pointing unit normal to the wall boundary (see Fig. 1). Motivated by the 2D level-set work in [18], Ren and E's slip condition can be extended to the general form

$$\beta(\phi)\mathbf{u}_s = -\left[\mathbf{n}\cdot\boldsymbol{\tau} + \sigma\delta_\epsilon(\phi)\left(\cos\theta_S - \frac{\nabla\phi\cdot\mathbf{n}}{|\nabla\phi|}\right)\nabla\phi\right]\cdot\mathbf{T}(\mathbf{n}), \tag{9}$$

where $\mathbf{u}_s = \mathbf{u} - \mathbf{u}_w$ is the slip velocity, θ_S is the prescribed static contact angle, $\beta(\phi) = \beta_N + \beta_{CL}\delta_\epsilon(\phi)|\nabla\phi\cdot\mathbf{T}(\mathbf{n})|$, β_N is the friction coefficient between the Newtonian fluids and the solid wall, and β_{CL} is the friction coefficient at the contact line. For any vector $\mathbf{a}$, $\mathbf{a}\cdot T(\mathbf{n})$ gives the tangential component of $\mathbf{a}$ in the plane with normal $\mathbf{n}$. Thus the right-hand side of (9) is a force (per unit area) tangential to the solid wall. This force includes contributions

from the viscous stress and the unbalanced Young's stress. It is obvious that $\mathbf{u}_s$ given by (9) is tangential to the wall since $\mathbf{u}_s \cdot \mathbf{n} = 0$. At the contact line, $\mathbf{u}_s$ is simply the contact line velocity relative to the solid wall. It should be noted that (9) has no limitation on spatial dimensions and it reduces to the boundary condition in [18] in 2D.

In the limit of vanishing ϵ, (9) recovers the 3D version of the Navier slip condition

$$\beta_N \mathbf{u}_s = -(\mathbf{n} \cdot \boldsymbol{\tau}) \cdot \mathbf{T}(\mathbf{n}) \tag{10}$$

away from the contact line (i.e., $\phi \neq 0$) and

$$\beta_{CL} \mathbf{u}_s = -\sigma \left(\cos\theta_S - \cos\theta_D\right) \frac{\nabla\phi \cdot \mathbf{T}(\mathbf{n})}{|\nabla\phi \cdot \mathbf{T}(\mathbf{n})|} \tag{11}$$

at the contact line (i.e., $\phi = 0$), where θ_D is the microscopic dynamic contact angle and we have used the geometric relation $\cos\theta_D = \mathbf{n}_\phi \cdot \mathbf{n} = \frac{\nabla\phi \cdot \mathbf{n}}{|\nabla\phi|}$. The term $\sigma\left(\cos\theta_S - \cos\theta_D\right)$ is exactly the unbalanced Young's stress [6]. In a 2D flow as shown in Fig. 1, these two equations reduce to the familiar formulations in [6, 18]:

$$\beta_N u_s = \mathbf{n} \cdot \boldsymbol{\tau} \cdot \mathbf{t} = \mu \frac{\partial u}{\partial y} \tag{12}$$

away from the contact line and

$$\beta_{CL} u_s = \sigma \left(\cos\theta_S - \cos\theta_D\right) \tag{13}$$

at the contact line, where u_s is the slip velocity in x-direction, $\mathbf{t}$ is the unit tangent vector to the wall, and u is the x-component of fluid velocity.

The Navier slip condition (12) determines a slip length $l_s = \frac{\mu}{\beta_N}$. Similar to viscosity, the phenomenological parameter β_N may take different values in the two fluids, although we will use a single constant in this paper for simplicity. Equation (13) agrees with the molecular-kinetic theory at the leading order [42]. It should be noted that β_N and β_{CL} have different dimensions.

A numerical advantage of the slip condition (9) is that it does not require us to manually impose the contact angle condition on the geometry of the interface. Instead, both the slip velocity $\mathbf{u}_s$ and the dynamic contact angle θ_D are part of the solution. If the contact line is at static equilibrium, both viscous stress $\boldsymbol{\tau}$ and $\mathbf{u}_s$ vanish and (9) recovers the static contact angle, i.e., $\theta_D = \theta_S$. If the contact line moves, then the relation (13) at the contact line predicts a θ_D that differs from θ_S. In particular, $\theta_D > \theta_S$ if the contact line advances and $\theta_D < \theta_S$ is the contact line recedes.

In summary, the governing equations include the level-set equation (1) for the interface and the Navier-Stokes equations (6) and (7) for the flow field, with the latter supplemented by the slip condition (9).

2.2. Level-set reinitialization

It is preferable that the level-set function ϕ is a signed distance function satisfying the Eikonal equation $|\nabla\phi| = 1$ in simulations. However, in the process of advection, ϕ could become too flat or too steep and cause large errors in computations. To prevent this, the level-set function needs to be reinitialized to a signed distance function regularly without altering the position of the interface. There are a lot of methods to achieve this goal and we use a PDE-based method that is discretized by a discontinuous Galerkin (DG) method. In the following, we briefly introduce this method and more details can be found in [43].

The PDE-based method, first proposed by Sussman *et al.* [40], is to evolve the Hamilton-Jacobi (HJ) equation

$$\phi_\tau + H(\nabla\phi) = 0 \text{ in } \Omega \times [0,T], \quad \phi(\mathbf{x},0) = \phi_0(\mathbf{x}) \tag{14}$$

to steady state, where τ is the pseudo time, ϕ_0 is the initial level-set function, $H(\nabla\phi) = S_\eta(\phi_0)\,(|\nabla\phi| - 1)$, $S_\eta(\phi_0) = \frac{\phi_0}{\sqrt{\phi_0^2+\eta^2}}$ is a smooth sign function, and η is a smoothing parameter usually chosen to be the computational mesh size $h_{\min}$ at the interface. Theoretically, ϕ shares the same zero level set with ϕ_0 and achieves $|\nabla\phi| = 1$ at the steady state. Instead of solving (14) for ϕ directly, we solve for $\nabla\phi$ first and then recover ϕ based on the exact location of the zero level set, as described in the following.

Let ϕ_h be an approximation of ϕ in a finite dimensional DG space. In each computational cell K, we have

$$\phi_h = \sum_{i=0}^{m} c_i v_i,$$

where c_i's are unknown coefficients, v_i's are basis polynomials, and m is the number of degrees of freedom. We choose Legendre polynomials such that v_0 is a constant. For convenience, we set $v_0 = 1$. Then the solution ϕ can be constructed based on

$$\nabla\phi_h = \sum_{i=1}^{m} c_i \nabla v_i$$

and an additive constant c_0.

Let I_p be the set of interface cells with sufficient length of interface inside. We first compute $\nabla\phi_h$ in these interface cells by a weighted local projection (WLP) method. In each cell $K \in I_p$, we obtain $\nabla\phi_h$ by minimizing the functional

$$\frac{1}{2}\int_K \left(\nabla\phi_h - \frac{\nabla\phi_0}{|\nabla\phi_0|}\right)^2 \bar{\delta}_\xi(\phi_0)\mathrm{d}\mathbf{x} + \frac{\lambda}{4}\int_K \left(|\nabla\phi_h|^2 - 1\right)^2 \mathrm{d}\mathbf{x}, \qquad (15)$$

where λ is a positive penalty parameter that enforces $|\nabla\phi_h| = 1$. $\bar{\delta}_\xi$ is a shifted smooth delta function defined as $\bar{\delta}_\xi(\phi) = \delta_\xi(\phi) + \xi_1$, where the half bandwidth ξ is usually a fraction of $h_{\min}$ and ξ_1 is a small positive parameter to avoid singular matrices. The nonlinear system after finite-element discretization is solved by Newton's method. Projecting $\nabla\phi_0$ is more accurate than projecting ϕ_0, since ϕ_0 varies along the normal direction to the interface while $\nabla\phi_0$ is nearly constant.

We then compute $\nabla\phi_h$ in all other cells by solving the gradient of (14)

$$\frac{\partial\nabla\phi}{\partial\tau} + \nabla H(\nabla\phi) = 0, \text{ in } \Omega\times[0,T], \quad \nabla\phi(\mathbf{x},0) = \nabla\phi_0(\mathbf{x}), \qquad (16)$$

as a conservation law system using a DG method following [44]. It should be noted the Lax-Friedrichs flux can not efficiently dissipate away the jump in the tangential component of $\nabla\phi$ on cell edges. We therefore constructed a hybrid numerical flux that combines the local Lax-Friedrichs flux and the penalty flux in [43].

Now we only need to find c_0 in each cell to fully recover ϕ_h. This is done in two steps. We first compute c_0 in all interface cells based on the interface location. In each interface cell, we find the intersections of $\phi_0 = 0$ with the cell edges and solve a least squares problem to determine the optimal c_0 such that the resulting $\phi_h = 0$ intersects the cell edges at almost the same intersections. This operation preserves the location of the zero level set. We then compute c_0 in all non-interface cells based on the continuity of ϕ_h between neighboring cells. More specifically, c_0 in each cell is determined based on its upwind neighbor. This requires the c_0 to be updated following the characteristics such that the upwind cells are always computed before their downwind neighbors.

This reinitialization method preserves interface very well and can achieve high-order accuracy. Another advantage of this method is the simple treatment of boundary conditions for contact line problems. When an interface intersects with a solid wall, boundary conditions are required for reinitial-

ization on the wall portion where

$$S_\eta(\phi_0)\frac{\nabla\phi}{|\nabla\phi|}\cdot\mathbf{n}<0.$$

Since we compute $\nabla\phi_h$ directly, we only need to supply a Dirichlet condition for $\nabla\phi$ based on the contact angle, which is much easier than the boundary condition for ϕ. In 3D, the boundary condition for $\nabla\phi$ can be obtained by solving an extension equation on the solid wall similar to that in [45].

2.3. Weak form of Navier-Stokes equations

In this subsection, we derive the weak form of the Navier-Stokes equations (6) and (7) supplemented with the slip condition (9).

Assume that the domain boundary $\partial\Omega$ can be partitioned into three parts based on boundary conditions: $\partial\Omega_D$ where the Dirichlet condition $\mathbf{u}=\mathbf{u}_b$ is imposed, $\partial\Omega_N$ where the traction condition (natural boundary condition) is imposed, and the solid wall $\partial\Omega_w$ where the no-penetration condition and slip condition are imposed. We seek the weak solution $(\mathbf{u},p)\in\mathcal{U}\times\mathcal{P}$, with solution spaces

$$\mathcal{U}=\{\mathbf{u}\in H^1(\Omega)^d:\mathbf{u}=\mathbf{u}_b \text{ on } \partial\Omega_D,\mathbf{u}\cdot\mathbf{n}=\mathbf{u}_w\cdot\mathbf{n} \text{ on } \partial\Omega_w\},\tag{17}$$

and

$$\mathcal{P}=L^2(\Omega)^d,\tag{18}$$

where d denotes the spatial dimension of the flow. The corresponding test spaces are

$$\mathcal{U}_0=\{\mathbf{u}\in H^1(\Omega)^d:\mathbf{u}=\mathbf{0} \text{ on } \partial\Omega_D,\mathbf{u}\cdot\mathbf{n}=0 \text{ on } \partial\Omega_w\},\tag{19}$$

and $\mathcal{P}$, respectively.

Taking the inner product of (6) with the test function $\mathbf{v}\in\mathcal{U}_0$ and the inner product of (7) with $q\in\mathcal{P}$ in Ω, we obtain the weak form

$$\begin{aligned}\left(\rho\left(\frac{\partial\mathbf{u}}{\partial t}+\mathbf{u}\cdot\nabla\mathbf{u}\right),\mathbf{v}\right)&=\left(\mathbf{n}\cdot\left(-p\mathbf{I}+\boldsymbol{\tau}+\boldsymbol{\tau}_\phi\right),\mathbf{v}\right)_{\partial\Omega}\\&\quad+(p,\nabla\cdot\mathbf{v})-(\boldsymbol{\tau}+\boldsymbol{\tau}_\phi,\nabla\mathbf{v})+(\rho\mathbf{g},\mathbf{v}),\quad\forall\mathbf{v}\in\mathcal{U}_0\end{aligned}\tag{20}$$

and

$$(\nabla\cdot\mathbf{u},q)=0,\quad\forall q\in\mathcal{P},\tag{21}$$

where $(\cdot,\cdot)$ denotes the inner product in Ω and $(\cdot,\cdot)_{\partial\Omega}$ denotes the inner product on $\partial\Omega$.

The boundary inner product on the right-hand side of (20) can be further written as

$$
\begin{aligned}
&\left(\mathbf{n}\cdot\left(-p\mathbf{I}+\boldsymbol{\tau}+\boldsymbol{\tau}_\phi\right),\mathbf{v}\right)_{\partial\Omega} && (22)\\
=&\left(\mathbf{n}\cdot\left(-p\mathbf{I}+\boldsymbol{\tau}+\boldsymbol{\tau}_\phi\right),\mathbf{v}\right)_{\partial\Omega_w} && (23)\\
=&\left(-\mathbf{n}p+\mathbf{n}\cdot\boldsymbol{\tau}+\sigma\delta_\epsilon(\phi)|\nabla\phi|\mathbf{n}\cdot(\mathbf{I}-\mathbf{n}_\phi\otimes\mathbf{n}_\phi),\mathbf{v}\right)_{\partial\Omega_w} && (24)\\
=&\left(\mathbf{n}\cdot\boldsymbol{\tau}-\sigma\delta_\epsilon(\phi)(\mathbf{n}\cdot\mathbf{n}_\phi)\nabla\phi,\mathbf{v}\right)_{\partial\Omega_w}, && (25)
\end{aligned}
$$

where we have used $\mathbf{v}=\mathbf{0}$ on $\partial\Omega_D$ and zero traction $\mathbf{n}\cdot(-p\mathbf{I}+\boldsymbol{\tau}+\boldsymbol{\tau}_\phi)=\mathbf{0}$ on $\partial\Omega_N$ in the first equality, and $\mathbf{n}\cdot\mathbf{v}=0$ on $\partial\Omega_w$ in the third equality. Here we consider zero traction for simplicity and an additional boundary inner product should be considered if the traction on $\partial\Omega_N$ is nonzero. Considering the slip condition (9), Eq. (20) can be further written as

$$
\begin{aligned}
\left(\rho\left(\frac{\partial\mathbf{u}}{\partial t}+\mathbf{u}\cdot\nabla\mathbf{u}\right),\mathbf{v}\right)+\beta(\phi)\left(\mathbf{u}-\mathbf{u}_w,\mathbf{v}\right)_{\partial\Omega_w}=&-\left(\sigma\delta_\epsilon(\phi)\cos\theta_S\nabla\phi,\mathbf{v}\right)_{\partial\Omega_w}\\
&+(p,\nabla\cdot\mathbf{v})-(\boldsymbol{\tau}+\boldsymbol{\tau}_\phi,\nabla\mathbf{v})+(\rho\mathbf{g},\mathbf{v}),\quad\forall\mathbf{v}\in\mathcal{U}_0. \quad (26)
\end{aligned}
$$

The weak solution $(\mathbf{u},p)$ can be found by solving (26) and (21).

2.4. Numerical methods

The governing equations are solved by the finite element method on a quadrilateral mesh with hierarchical adaptive mesh refinement based on the open-source deal.II library [46, 47]. Due to different natures of these equations, we solve the level-set equation and the Navier-Stokes equations separately with the former solved by DG and the latter solved by the mixed finite element method.

We focus on 2D problems. Consider a triangulation $\mathcal{T}_h$, consisting of non-overlapping quadrilaterals, of the computational domain Ω. We define the discontinuous finite-element space

$$
V_D^N=\{\phi:\phi\in P^N(K),\forall K\in\mathcal{T}_h\} \quad (27)
$$

and continuous finite-element space

$$
V_C^N=\{\phi\in C^0(\Omega):\phi\in Q^N(K),\forall K\in\mathcal{T}_h\}, \quad (28)
$$

where N denotes the polynomial degree. In this work, we take $N=3$ for ϕ, $N=2$ for $\mathbf{u}$, and $N=1$ for p. The finite dimensional solution spaces for ϕ_h, $\mathbf{u}_h$, and p_h are $\mathcal{F}_h=V_D^3$, $\mathcal{U}_h=\left(V_C^2\right)^2\cap\mathcal{U}$, and $\mathcal{P}_h=V_C^1$, respectively, where

we have used the subscript $_h$ to denote finite-dimensional approximations. The test space for $\mathbf{u}_h$ is simply $\mathcal{U}_{h,0} = \left(V_C^2\right)^2 \cap \mathcal{U}_0$.

Since the flow is incompressible, the level-set equation (1) can be written as a conservation law

$$\frac{\partial \phi}{\partial t} + \nabla \cdot (\mathbf{u}\phi) = 0. \tag{29}$$

In each element K, by taking the inner product of (29) with the test function $\psi \in \mathcal{F}_h$ and performing integration by parts, we obtain the weak formulation

$$\left(\frac{\partial \phi_h}{\partial t}, \psi\right)_K + \left(\hat{H}(\phi_h^-, \phi_h^+), \psi\right)_{\partial K} - (\mathbf{u}_h \phi_h, \nabla \psi)_K = 0, \quad \forall \psi \in \mathcal{F}_h, \tag{30}$$

where $\hat{H}(\phi_h^-, \phi_h^+)$ denotes the numerical flux that approximates $\mathbf{n} \cdot \mathbf{u}_h \phi_h$, ϕ_h^- and ϕ_h^+ are the inside and outside values of ϕ_h on the element boundary ∂K, and $\mathbf{n}$ is the outward pointing unit normal to ∂K. We use the local Lax-Friedrichs flux

$$\hat{H}(\phi_h^-, \phi_h^+) = \mathbf{n} \cdot \mathbf{u}_h \frac{\phi_h^- + \phi_h^+}{2} - \frac{\alpha}{2}(\phi_h^+ - \phi_h^-), \tag{31}$$

where $\alpha = \max(|\mathbf{n} \cdot \mathbf{u}_h|)$ and the maximum is taken over the relevant element edge. The semi-discrete weak form (30) is integrated by the third-order total variation diminishing (TVD) Runge-Kutta (RK) method [48] to advance ϕ_h^n to ϕ^{n+1}. To decouple $\mathbf{u}_h$ from ϕ_h, the $\mathbf{u}_h$ values at intermediate time levels between t^n and t^{n+1}, which are required by the TVD RK method, are obtained by explicit extrapolations from $\mathbf{u}_h^{n-1}$ and $\mathbf{u}_h^n$. Note that we choose the third-order TVD RK for the sake of stability rather than accuracy, and the overall scheme is only second-order accurate in time.

The discontinuous solution ϕ_h cannot be differentiated. We thus map it to a continuous function $\phi_C \in V_C^3$ by least squares before feeding it to flow equations:

$$(\phi_C - \phi_h, \psi) = 0, \quad \forall \psi \in V_C^3. \tag{32}$$

The flow equations (26) and (21) are discretized by the Crank-Nicolson scheme. In each time step, we seek the weak solution $(\mathbf{u}_h^{n+1}, p_h^{n+\frac{1}{2}}) \in \mathcal{U}_h \times \mathcal{P}_h$

satisfying the discretized weak form

$$\begin{aligned}
&\left(\rho(\phi_C^{n+\frac{1}{2}})\left(\tfrac{\mathbf{u}_h^{n+1}-\mathbf{u}_h^n}{\Delta t}+\mathbf{u}_h^*\cdot\nabla\mathbf{u}_h^{n+\frac{1}{2}}+\tfrac{1}{2}(\nabla\cdot\mathbf{u}_h^*)\mathbf{u}_h^{n+\frac{1}{2}}\right),\mathbf{v}\right)\\
&+\beta(\phi_C^{n+\frac{1}{2}})\left(\mathbf{u}_h^{n+\frac{1}{2}}-\mathbf{u}_w,\mathbf{v}\right)_{\partial\Omega_w}=-\left(\sigma\delta_\epsilon(\phi_C^{n+\frac{1}{2}})\cos\theta_S\nabla\phi_C^{n+\frac{1}{2}},\mathbf{v}\right)_{\partial\Omega_w}\\
&\qquad+\left(p_h^{n+\frac{1}{2}},\nabla\cdot\mathbf{v}\right)-\left(\mu(\phi_C^{n+\frac{1}{2}})(\nabla\mathbf{u}_h^{n+\frac{1}{2}}+(\nabla\mathbf{u}_h^{n+\frac{1}{2}})^T),\nabla\mathbf{v}\right)\\
&-\left(\sigma\delta_\epsilon(\phi_C^{n+\frac{1}{2}})\left|\nabla\phi_C^{n+\frac{1}{2}}\right|(\mathbf{I}-\mathbf{n}_\phi^{n+\frac{1}{2}}\otimes\mathbf{n}_\phi^{n+\frac{1}{2}}),\nabla\mathbf{v}\right)+(\rho(\phi_C^{n+\frac{1}{2}})\mathbf{g},\mathbf{v}),\quad\forall\mathbf{v}\in\mathcal{U}_{h,0}
\end{aligned}\tag{33}$$

and

$$-(\nabla\cdot\mathbf{u}_h^{n+1},q)=0,\quad\forall q\in\mathcal{P}_h,\tag{34}$$

where $\mathbf{u}_h^{n+\frac{1}{2}}=\frac{\mathbf{u}_h^n+\mathbf{u}_h^{n+1}}{2}$, $\phi_C^{n+\frac{1}{2}}=\frac{\phi_C^n+\phi_C^{n+1}}{2}$, $\mathbf{n}_\phi^{n+\frac{1}{2}}=\frac{\nabla\phi_C^{n+\frac{1}{2}}}{\left|\nabla\phi_C^{n+\frac{1}{2}}\right|}$, and $\mathbf{u}_h^*$ is an explicit approximation of $\mathbf{u}^{n+\frac{1}{2}}$ by a linear extrapolation from $\mathbf{u}_h^n$ and $\mathbf{u}_h^{n-1}$. Here we have adopted the skew-symmetric form for the convection term and the scheme is unconditionally stable if the density is a constant.

Thanks to the explicit approximation $\mathbf{u}_h^*$, Eqs. (33) and (34) lead to a linear saddle point problem:

$$\begin{bmatrix}A & B^T\\ B & 0\end{bmatrix}\begin{bmatrix}U\\ P\end{bmatrix}=\begin{bmatrix}F\\ 0\end{bmatrix},\tag{35}$$

where U and P are solution vectors for $\mathbf{u}_h^{n+1}$ and $p_h^{n+\frac{1}{2}}$, respectively. The asymmetric square block A comes from (33) excluding the pressure term while the non-square block B comes from (34). In this paper, we only consider two dimensional problems. The size of the resulting matrix is relatively small, and we solve (35) by the direct sparse linear solver UMFPACK [49].

In each time step, the solution procedure can be summarized as follows:

(i) Check the mesh and the interface. If necessary, perform local refinement and coarsening such that the interface region is covered by the finest mesh and bulk region is covered by the coarsest mesh. Transfer data from the old mesh to the new mesh if the mesh is altered.
(ii) Based on $\mathbf{u}_h^n$, $\mathbf{u}_h^{n-1}$, and ϕ_h^n, solve (30) to obtain ϕ_h^{n+1}.
(iii) Reinitialize ϕ_h^{n+1} to a signed distance function if necessary.
(iv) Map ϕ_h^{n+1} to ϕ_C^{n+1} in the continuous finite space by solving (32).

(v) Based on $\mathbf{u}_h^n$, $\mathbf{u}_h^{n-1}$, ϕ_C^n, and ϕ_C^{n+1}, solve the linear system of (33) and (34) to obtain $\mathbf{u}_h^{n+1}$ and $p_h^{n+\frac{1}{2}}$.

3. Contact angle hysteresis

With the contact angle hysteresis, the contact line remains pinned for a range of contact angles, the minimum of which is referred to as the receding contact angle θ_R and the maximum is referred to as the advancing contact angle θ_A. The contact line advances if $\theta_D > \theta_A$, recedes if $\theta_D < \theta_R$, and is pinned if $\theta_R \le \theta_D \le \theta_A$.

When the contact line moves, we can still use the method in the previous section with θ_S replaced by θ_A for the advancing contact line and by θ_R for the receding contact line. Special treatment is needed when the contact line is pinned. In this case, the no-slip condition $\mathbf{u}_s = \mathbf{0}$ is required at the contact line. To make this condition consistent with (9), we adopt the formula

$$\beta(\phi)\mathbf{u}_s = -(\mathbf{n}\cdot\boldsymbol{\tau})\cdot\mathbf{T}(\mathbf{n}), \tag{36}$$

which recovers the no-slip condition at $\phi = 0$ while still maintaining the Navier slip condition away from the contact line. Thus it provides a smooth transition between the pinned and moving contact lines. With (36) in place of (9), the weak form of the momentum equation (26) is updated to

$$\begin{aligned}\left(\rho\left(\frac{\partial\mathbf{u}}{\partial t}+\mathbf{u}\cdot\nabla\mathbf{u}\right),\mathbf{v}\right)+\beta(\phi)\left(\mathbf{u}-\mathbf{u}_w,\mathbf{v}\right)_{\partial\Omega_w} &= -\left(\sigma\delta_\epsilon(\phi)\frac{\nabla\phi\cdot\mathbf{n}}{|\nabla\phi|}\nabla\phi,\mathbf{v}\right)_{\partial\Omega_w}\\ &\quad+(p,\nabla\cdot\mathbf{v})-(\boldsymbol{\tau}+\boldsymbol{\tau}_\phi,\nabla\mathbf{v})+(\rho\mathbf{g},\mathbf{v}),\quad\forall\mathbf{v}\in\mathcal{U}_0.\end{aligned} \tag{37}$$

when the contact line is pinned. It should be noted that the only difference between this equation and (26) is the first term on the right-hand side: $\cos\theta_S$ in the inner product on $\partial\Omega_w$ is now replaced by $\cos\theta_D = \frac{\nabla\phi\cdot\mathbf{n}}{|\nabla\phi|}$.

The relation between θ_D and (θ_R, θ_A) can be inferred from ϕ. Motivated by the phase-field method for hysteresis in [38], we define

$$F(\theta) = \int_e \delta_\epsilon(\phi)\left(\cos\theta - \frac{\nabla\phi\cdot\mathbf{n}}{|\nabla\phi|}\right)\mathrm{dS}, \tag{38}$$

where e is an element edge (element face in 3D) in the neighborhood of the contact line on $\partial\Omega$. Obviously, $\theta_D > \theta$ if $F(\theta) > 0$ and $\theta_D < \theta$ if $F(\theta) < 0$. Then the status (advancing, receding, or pinned) of the contact line can be determined from the signs of $F(\theta_A)$ and $F(\theta_R)$.

In the first term on the right-hand side of the discretized weak form (33), we need to perform integration on the boundary edges on $\partial\Omega_w$. The contact angle hysteresis can be incorporated with a little modification to this boundary integral. For each element edge e on $\partial\Omega_w$, we first evaluate $F(\theta_A)$ and $F(\theta_D)$ with $\phi = \phi_C^{n+\frac{1}{2}}$ in (38), and then proceed as follows with boundary inner product in (33):

- If $F(\theta_A) > 0$, then $\theta_D > \theta_A$ and the contact line advances. Set $\theta_S = \theta_A$.
- If $F(\theta_R) < 0$, then $\theta_D < \theta_R$ and the contact line recedes. Set $\theta_S = \theta_R$.
- Otherwise, $\theta_A \geq \theta_D \geq \theta_R$ and the contact line is pinned. Set $\cos\theta_S = \frac{\nabla\phi_C^{n+\frac{1}{2}} \cdot \mathbf{n}}{\left|\nabla\phi_C^{n+\frac{1}{2}}\right|}$, i.e., $\theta_S = \theta_D$.

Since $\theta_A > \theta_D$, we have $\cos\theta_A < \cos\theta_D$ and the third case corresponds to $F(\theta_R) \geq 0 \geq F(\theta_A)$. These operations are performed on all boundary edges on $\partial\Omega_w$; but only the boundary integral on the edges in the contact line region, i.e., where $\delta_\epsilon(\phi)$ is non-zero, is affected. All the other operations remain the same as those in Section 2.4. Thus, the contact angle hysteresis can be easily included in the formulation for moving contact line problems.

In our method, whether the contact line is pinned or not, the dynamic angle θ_D is computed from the momentum equation and thus the momentum balance is automatically satisfied. There is no need to use any special technique as in [35] to determine θ_D that satisfies local momentum balance when the contact line is pinned.

It should be noted that β_{CL} for the pinned contact line essentially plays a role of penalty parameter to enforce the no-slip condition. Thus, in order to achieve a good pinning performance, we may need to choose a large enough β_{CL} for the pinned contact line. In other words, we need a large contact line friction to resist contact line motion and thus pin the contact line.

4. Numerical results and discussions

We consider six test cases. We first validate the interfacial flow part of our code by computing a bubble rising problem. In the test case of an advancing interface in plane Poiseuille flow, we systematically investigate the use of Ren and E's slip condition in moving contact line problems including mesh convergence and parameter justification. In the test case of drop

spreading, we come up with a computational strategy for predictive simulations. In the test case of a pinned drop in plane Poiseuille flow, we validate the capability of our method in pinning the contact lines. In the test case of advancing and receding interfaces in plane Poiseuille flow, we demonstrate that our method correctly captures the transition between pinning and moving. Finally, in the test case of sliding drop on an inclined wall, we further demonstrate the capability of our method in capturing hysteresis. All the parameters are dimensionless except for the bubble rising problem.

4.1. Bubble rising

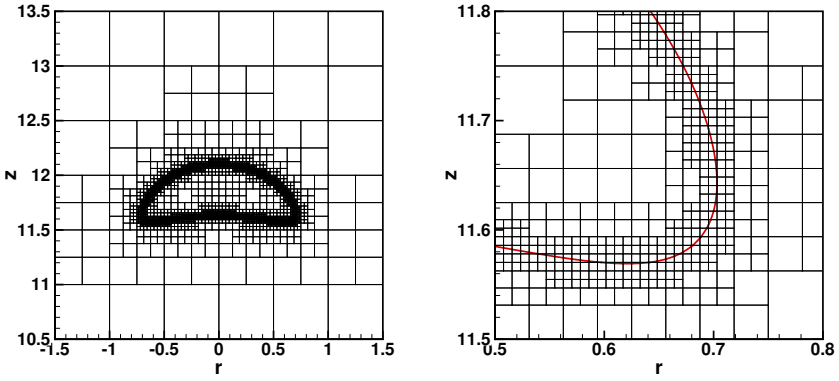

Figure 2: Illustration of the adaptive mesh refinement. The left panel shows the mesh around the bubble while the right panel shows a close-up view at the rim of the bubble. The thick solid (red) line in the right panel denotes the interface, i.e., the $\phi = 0$ level set.

Hnat and Buckmaster conducted experiments with spherical-cap air bubbles rising in incompressible liquids to study the steady-state shapes and terminal velocities [50], wherein the results were reproduced numerically by many others [51, 52, 53, 54, 55] for code validation. In this numerical test, we will use the experiment of Fig. 1a in [50] with the following parameters: liquid density $\rho_l = 0.8755$ g cm^{-3}, gas density $\rho_g = 0.001$ g cm^{-3}, liquid viscosity $\mu_l = 1.18$ P, gas viscosity $\mu_g = 0.01$ P, surface tension $\sigma = 32.2$ dyn cm^{-1}, gravitation acceleration $g = 980$ cm s^{-2}, and bubble radius $R_0 = 0.61$ cm. Due to axisymmetry, we only compute the right half of the meridian plane. In the r-z plane, the computational domain is a rectangle of $(0, 8R_0) \times (0, 30R_0)$ and the initially spherical bubble is released from $(0, 5R_0)$. We use an adaptive mesh with minimum mesh size $h_{\min} = \frac{R_0}{64}$ at

the interface and maximum mesh size $h_{\max} = R_0$ far away from the bubble, as shown in Fig. 2. The half-width of the interface is taken to be $\epsilon = 1.5h_{\min}$.

Our numerical results are displayed in Fig. 3. The bubble shape and the wake structure at the steady state are in good agreement with the experiment, as shown in Fig. (3a). We also keep track of the instantaneous velocities at the top and the bottom of the bubble, which are shown in Fig. (3b). The steady-state velocity in our numerical test, which is 21.89 cm s^{-1}, is slightly larger than 21.5 cm s^{-1} reported by the experiments. We note that a similar terminal speed, 21.90 cm s^{-1}, was obtained in [52].

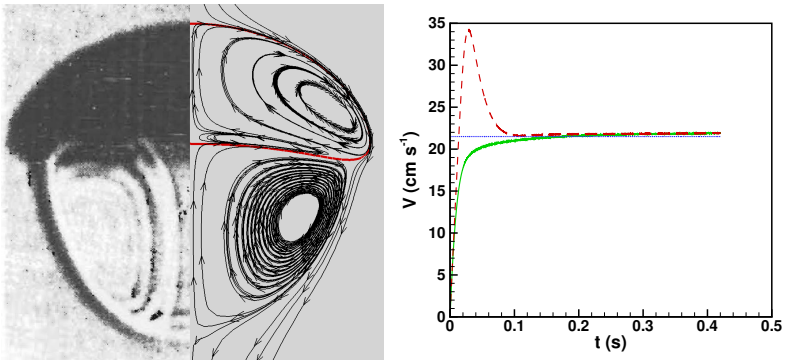

(a) (b)

Figure 3: The steady-state bubble shape (a) and the instantaneous velocities at the top and the bottom of the bubble (b). The left half of (a) is the experimental image adapted from [50].

4.2. Advancing interface in plane Poiseuille flow

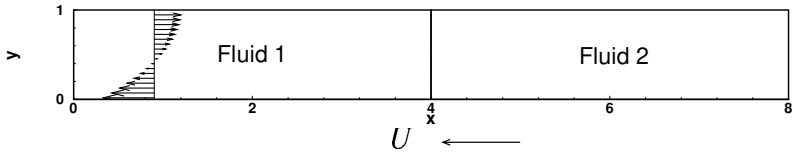

Figure 4: schematic of an advancing interface in plane Poiseuille flow.

We consider the steady plane Poiseuille flow of two immiscible fluids with identical viscosity μ. Inertia is neglected. The frame is fixed to the interface, i.e., the walls are moving horizontally with constant speed U while the interface is stationary. In the following, all numbers are made dimensionless

by channel half width W, surface tension σ, and fluid viscosity μ, unless otherwise specified. Under this normalization, we have $W = \sigma = \mu = 1$. Since the flow is symmetric, we only compute the lower half of the channel. The computational domain is a rectangle of $(0, 8) \times (0, 1)$ in the x-y plane, with $y = 0$ being the moving wall and $y = 1$ being the axis of symmetry, as shown in Fig. 4. We run the simulation with an initially flat interface at $x = 4$ until a steady state is achieved. The capillary number is defined as $Ca = \mu U/\sigma$. We first investigate mesh convergence of our method and then analyze the variables that affect contact line dynamics.

4.2.1. Mesh convergence

Mesh convergence is crucial to all predictive numerical simulations. This task gets more challenging with a moving contact line: the slip length has to be well resolved to produce mesh-independent results [56, 33, 26]. It should be noted that all mesh-based numerical results cannot be exactly mesh-independent. We borrow this term "mesh-indepenet" from [26] to denote that the results are insensitive to the mesh size. There are three microscopic length scales: mesh size $h_{\min}$, (half) thickness of the interface ϵ, and slip length l_s. Here, only l_s is physically relevant and the other two are numerical. Our goal is to find a way to generate results that are independent of $h_{\min}$ and ϵ.

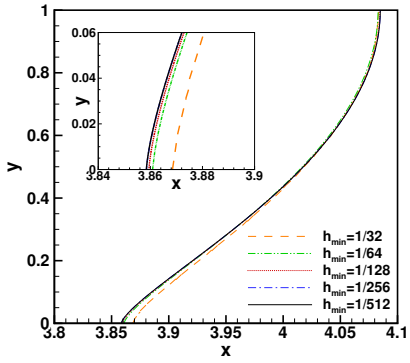

Figure 5: Mesh convergence for a fixed interface thickness. The inset is a close-up view at the contact line. $\epsilon = \frac{1.5}{128}$, $\beta_N = 100$ (such that $l_s = 0.01$), $\beta_{CL} = 1$, $Ca = 0.03$, $\theta_S = 90°$.

These lengths define two independent dimensionless groups, eg., $\frac{h_{\min}}{\epsilon}$ and $\frac{\epsilon}{l_s}$. We first investigate $\frac{h_{\min}}{\epsilon}$, i.e., how to choose mesh size to achieve mesh convergence for a given interfacial thickness. We fix the interfacial

thickness at $\epsilon = \frac{1.5}{128}$, and conduct simulations with $h_{\min} = \frac{1}{32}, \frac{1}{64}, \cdots, \frac{1}{512}$, which corresponds to $\frac{\epsilon}{h_{\min}} = 0.375, 0.75, \cdots, 6$. The slip length is taken to be $l_s = 0.01$, which is well resolved by ϵ as explained later. We can easily see the convergence in the steady-state interface profile, as shown in Fig. 5, as $h_{\min}$ reduces. The curves of $h_{\min} = \frac{1}{256}$ and $\frac{1}{512}$ overlap; the errors are negligible even for $h_{\min} = 1/128$ and $h_{\min} = 1/64$. The result gets unsatisfactory when the mesh is coarsened to $h_{\min} = \frac{1}{32}$. We thus come to the first criterion for sufficient accuracy:

$$\frac{h_{\min}}{\epsilon} \leq \frac{4}{3}. \tag{39}$$

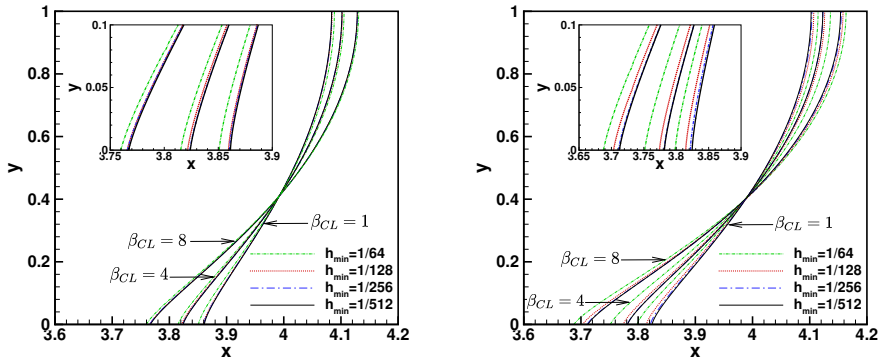

(a) $l_s = 0.01$ ($\beta_N = 100$) (b) $l_s = 0.005$ ($\beta_N = 200$)

Figure 6: Mesh convergence at fixed l_s and $\frac{h_{\min}}{\epsilon}$. The insets are close-up views at the contact line. $\epsilon = 1.5h_{\min}$, $Ca = 0.03$, $\theta_S = 90^\circ$.

	$\beta_{CL} = 1$		$\beta_{CL} = 4$		$\beta_{CL} = 8$	
$h_{\min}$	H	E_r	H	E_r	H	E_r
1/64	0.2373	6.76%	0.2893	4.26%	0.3444	2.96%
1/128	0.2249	1.17%	0.2806	1.13%	0.3364	0.56%
1/256	0.2235	0.54%	0.2778	0.11%	0.3356	0.34%
1/512	0.2223	0	0.2775	0	0.3345	0

Table 1: Relative errors in the height of the circular arc shaped interface. $\epsilon = 1.5h_{\min}$, $Ca = 0.03$, $\theta_S = 90^\circ$, $\beta_N = 100$. The height H is the distance in the x direction measured from the contact line to the apex of the interface. E_r is the relative error in H, where we have used the solution at $h_{\min} = \frac{1}{512}$ as the reference.

We next investigate $\frac{\epsilon}{l_s}$, i.e., the sharp-interface limit with respect to ϵ when l_s is fixed. We keep $\frac{h_{\min}}{\epsilon} = \frac{1}{1.5}$ fixed while refining mesh, such that ϵ is always well resolved. We test $\beta_N = 100$ and 200, which correspond to $l_s = 0.01$ and 0.005, respectively, as illustrated in Fig. 6. The detailed errors for $\beta_N = 100$ are given in Table 1. Curves with different β_{CL} show that this parameter does not affect mesh convergence. Convergence is achieved if $h_{\min} \leq \frac{1}{128}$ for $l_s = 0.01$ and $h_{\min} \leq \frac{1}{256}$ for $l_s = 0.005$. It is tempting to conclude a convergence criterion based on $\frac{h_{\min}}{l_s}$. However, the curve of $h_{\min} = \frac{1}{64}$ and $\epsilon = \frac{1.5}{128}$ in Fig. 5 shows much better convergence than that of $h_{\min} = \frac{1}{64}$ and $\epsilon = \frac{1.5}{64}$ in Fig. 6(a), which suggests $\frac{\epsilon}{l_s}$ to be a better choice. We thus have the second criterion for sufficient accuracy:

$$\frac{\epsilon}{l_s} \leq \frac{150}{128}. \tag{40}$$

In summary, we should choose the mesh size and the interface thickness according to $h_{\min} \lesssim \epsilon \lesssim l_s$ to obtain numerical results that are independent of $h_{\min}$ and ϵ. This looks very similar to the criterion for the sharp-interface limit in the phase-field method [57]. The advantage of the level-set method is that it does not require a lot of mesh cells across the narrow-band interface. In the rest of this paper, we conservatively choose $\epsilon = 1.5h_{\min}$ as suggested in [40] and make sure $l_s \geq 1.28h_{\min}$.

4.2.2. Contact line dynamics

The contact line dynamics in Ren and E's slip model is controlled by β_N, β_{CL}, and θ_S. The effect of θ_S is well understood, but it is still unclear how β_N and β_{CL} quantitatively affect contact line dynamics. Here we try to answer this question by comparing with the well-established Cox theory [31].

According to the matched asymptotic analysis by Cox, to the leading order, the apparent contact angle θ_{app} and the static contact angle θ_S are connected by

$$g(\theta_{app}) = g(\theta_S) + \mathrm{Ca}\ln(L/L_s) \tag{41}$$

due to viscous bending of the interface. Here L_s is the slip length that characterizes the inner region of the contact line and L is characteristic length of the macroscopic flow. Note that this L_s is a "physical" scale associated with the contact line and may be different from the l_s. To distinguish these two length scales, we refer to L_s as the effective slip length and l_s as the numerical slip length hereafter. For the plane Poiseuille flow, we can simply

take $L = W$. The function g is given by

$$g(\theta) = \int_0^\theta \frac{d\theta}{f(\theta)} \tag{42}$$

where

$$f(\theta, r_\mu) = \frac{2\sin\theta\left\{r_\mu^2(\theta^2-\sin^2\theta)+2r_\mu\left[\theta(\pi-\theta)+\sin^2\theta\right]+\left[(\pi-\theta)^2-\sin^2\theta\right]\right\}}{r_\mu(\theta^2-\sin^2\theta)[(\pi-\theta)+\sin\theta\cos\theta]+\left[(\pi-\theta)^2-\sin^2\theta\right](\theta-\sin\theta\cos\theta)} \tag{43}$$

and r_μ is the viscosity ratio between the receding and advancing fluids.

We first study the influence of Ca on θ_{app} and θ_D. Here θ_{app} is determined by fitting a circle to the deformed interface [58, 57] and θ_D is directly measured from the $\phi = 0$ level curve at the contact line. The results for various combinations of (β_N, β_{CL}) with fixed $\theta_S = 90^\circ$ are shown in Fig. 7. Figure 7(a) confirms that $g(\theta_{app})$ is linear in Ca, in accordance with the Cox theory (41). Not surprisingly, $g(\theta_D)$ is also a linear function of Ca, consistent with the numerical observation in [6] as well as the molecular-kinetic theory [59]. It should be noted that $g(\theta_S) = 0.1921$, which is exactly the $y-$intercept of both $g(\theta_{app})$ and $g(\theta_D)$.

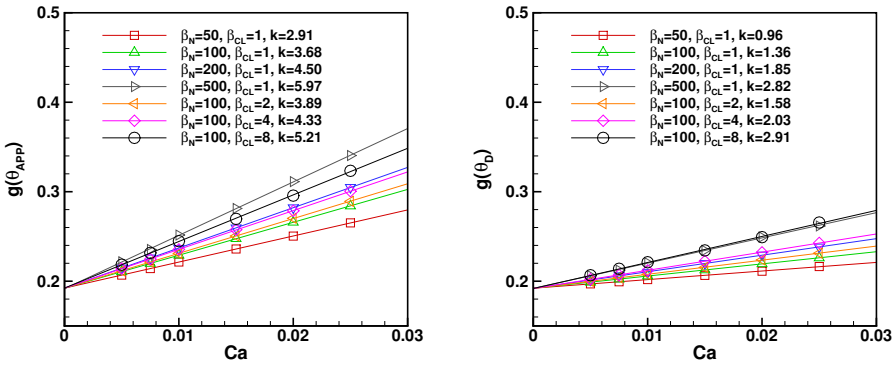

(a) (b)

Figure 7: Dependence of $g(\theta_{app})$ and $g(\theta_D)$ on Ca for different (β_N, β_{CL}). $\theta_S = 90^\circ$. The k values are the slopes of the linear fits.

This linear behavior is also observed for different θ_S, as shown in Fig. 8. According to (41), the slope of the $g(\theta_{app})$–Ca curve is only dependent on L_s and is independent of θ_S. This is confirmed by Fig. 8(a) with acceptable errors: the slopes have an average of 3.4 and a standard deviation of 0.3. The largest deviation from the average is observed for $\theta_S = 120^\circ$, possibly

because θ_{app} is too close to 180° and the circle fitting is more prone to numerical errors due to a larger interface deformation. Similar linear behavior is also observed for $g(\theta_D)$, as shown in Fig. 8(b), with an average slope of 1.31 and a standard deviation of 0.09.

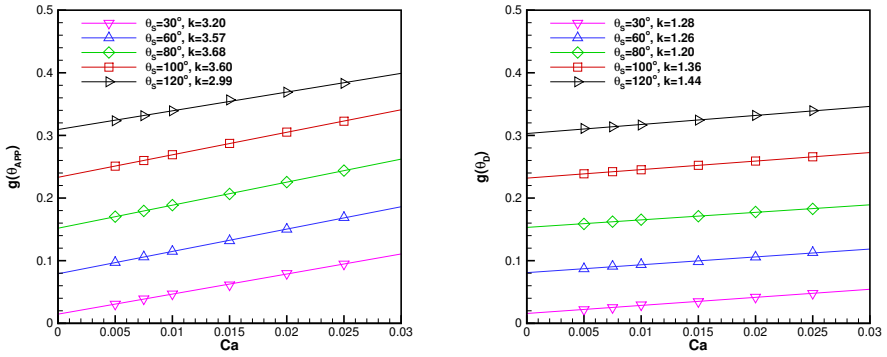

(a) (b)

Figure 8: Dependence of $g(\theta_{app})$ and $g(\theta_D)$ on Ca for different θ_S. $\beta_N = 100$, $\beta_{CL} = 1$.

The results in Figs. 7 and 8 suggest that both θ_{app} and θ_D can fit in the relation

$$g(\theta) = g(\theta_S) + Ca\, k, \tag{44}$$

where k is dependent on both β_N and β_{CL} but independent of θ_S. Comparing with (41), we can see that β_N and β_{CL} work together to determine the effective slip length L_s that controls the dynamics of θ_{app}. For example, in Fig. 7(a), the slope $k = 2.91$ for $(\beta_N, \beta_{CL}) = (50, 1)$ corresponds to $\frac{L_s}{W} = 0.055$, and the slope $k = 5.21$ for $(\beta_N, \beta_{CL}) = (100, 8)$ corresponds to $\frac{L_s}{W} = 0.0055$.

Since both θ_{app} and θ_D satisfy (44), it follows that

$$g(\theta_{app}) = g(\theta_D) + Ca\, \tilde{k}, \tag{45}$$

for some constant $\tilde{k}$, which is easily confirmed by numerical results. It is, however, surprising to note that this $\tilde{k}$ is independent of β_{CL}, as shown in Fig. 9. That is, β_{CL} has nothing to do with viscous bending. The data points for $\beta_{CL} = 1$ indicate that $\tilde{k} \approx 0.52 \ln\left(\frac{W}{l_s}\right)$, where $l_s = \frac{\mu}{\beta_N}$. We do not have any good explanation on the prefactor for now and will leave further investigation for future work.

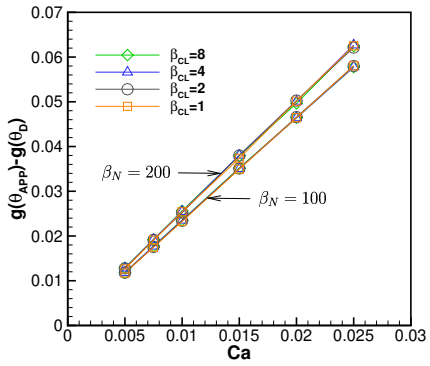

Figure 9: $g(\theta_{app}) - g(\theta_D)$ as a function of Ca. $\theta_S = 90°$.

In summary, β_N and β_{CL} both affect the deviation of θ_D from θ_S, while only β_N controls the viscous effect that bends the interface from θ_D at the wall to θ_{app} at the macroscopic scale. It is the cooperation of β_N and β_{CL} that determines the effective slip length L_s.

4.3. Drop spreading and computational strategy

In this subsection, we simulate two cases of drop spreading with different initial contact angles. Inertia is again neglected. The computational setup is illustrated in Fig. 10. The flow is axisymmetric and we only compute the right half of the median plane.

4.3.1. Comparison with the Cox theory

In the first test case, we consider the spreading of an initially hemispherical drop with radius $R_0 = 0.5$. We take $\theta_S = 60°$. The spreading radius will be directly compared with the theoretical results in [60].

If we assume the drop to be a spherical cap, which is a reasonable approximation for $Ca \ll 1$, the spreading radius a can be written as a function of θ_{app} based on volume conservation:

$$a = \left(\frac{3V_d}{\pi}\right)^{1/3} \frac{\sin\theta_{app}}{(2 - 3\cos\theta_{app} + \cos^3\theta_{app})^{1/3}}, \tag{46}$$

where V_d is the volume of the drop. The final spreading radius a_f can be predicted based on the static contact angle θ_S and the initial contact angle

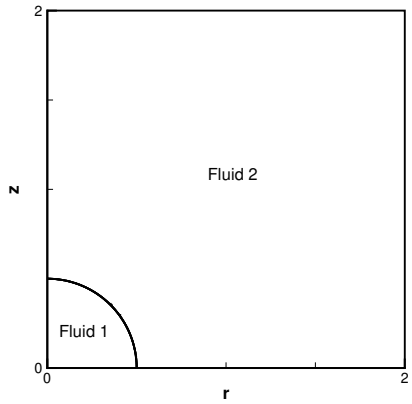

Figure 10: Computational setup for drop spreading simulations. The computation domain is a square of $4R_0 \times 4R_0$ with the wall located at $z = 0$.

θ_0 [60]:

$$\frac{a_f}{a_0} = \left[\frac{\left(2 - 3\cos\theta_0 + \cos^3\theta_0\right)\sin^3\theta_S}{\left(2 - 3\cos\theta_S + \cos^3\theta_S\right)\sin^3\theta_0} \right]^{1/3}, \tag{47}$$

where a_0 is the initial spreading radius. For the hemispherical drop considered here, we have $a_0 = R_0$ and $\theta_0 = 90^\circ$ and the equation above gives $\frac{a_f}{R_0} = 1.276186$ for $\theta_S = 60^\circ$, which is confirmed by our numerical results in Figs. 12.

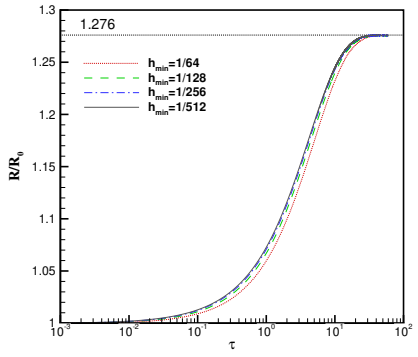

Figure 11: Mesh convergence for the drop spreading problem. $\theta_S = 60^\circ$, $r_\mu = 0.01$, $\beta_N = 100$, $\beta_{CL} = 1$, $\epsilon = 1.5h_{\min}$.

$h_{\min}$	a_f/R_0	E_r	order
1/64	1.275312	6.85E-04	-
1/128	1.275458	5.70E-04	0.26
1/256	1.275830	2.79E-04	1.03
1/512	1.276010	1.38E-04	1.02

Table 2: Maximal spreading radius at different levels of mesh refinement. E_r is the relative error in a_f compared against the theoretical value. $\theta_S = 60°$, $r_\mu = 0.01$, $\beta_N = 100$, $\beta_{CL} = 1$, $\epsilon = 1.5h_{\min}$.

The mesh convergence results for this transient problem are shown in Fig. 11. The different spreading curves converge as the mesh refines. The final spreading radii are given in Table 2, which indicates a first order convergence. This is expected due to the smooth Dirac delta function $\delta_\epsilon(\phi)$ in the formulation.

It was reported in [60] that the influence of gas viscosity is negligible for $r_\mu \leq 0.01$. We verify this by computing spreading with $r_\mu = 1, 0.1, \cdots, 0.0001$, and the numerical results are given in Fig. 12(a). It is obvious that the spreading curves with $r_\mu \leq 0.01$ are indistinguishable. In the following simulations we will simply use $r_\mu = 0.01$ for gas-liquid systems.

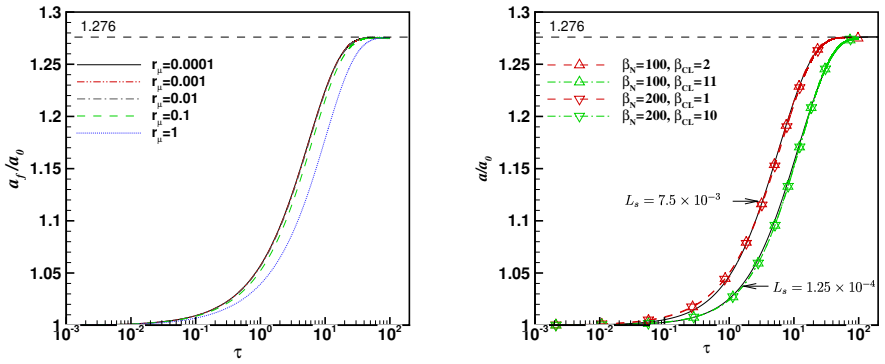

(a) Effect of viscosity ratio.

(b) Comparison with theory.

Figure 12: Spreading of a hemispherical drop with $\theta_S = 60°$. In (a), we vary the viscosity ratio r_μ while keeping $\beta_N = 100$ and $\beta_{CL} = 1$ fixed. In (b), we vary β_N and β_{CL} while keeping $r_\mu = 0.01$ fixed. The solid lines in (b) are theoretical curves based on the Cox theory with L_s labeled in the plot and $L = a_0$. The finest mesh size is set to $h_{\min} = \frac{1}{128}$ and $\frac{1}{256}$ for $\beta_N = 100$ and 200, respectively.

Based on the Cox theory, Wörner *et al.* [60] derived analytical equations to predict the $a \sim t$ curves of spherical-cap shaped drops. The effective

slip L_s of the moving contact line can thus be determined by matching the theoretical and the actual spreading curves. The spreading curves with different (β_N, β_{CL}) values are given in Fig. 12(b). First of all, the theoretical curves match the numerical ones very well if a proper L_s is chosen. Thus our level-set method with slip condition (9) agrees with the Cox theory. Meanwhile, the same L_s can be reproduced by multiple choices of (β_N, β_{CL}). This indicates that β_{CL} can be used to compensate β_N in controlling the effective slip L_s, and further motivates the following computational strategy. The overlap of transient curves with different (β_N, β_{CL}) also suggests that different choices of (β_N, β_{CL}) are able to produce the same amount of contact line dissipation.

4.3.2. Computational strategy

We propose the following computational strategy for mesh-independent and predictive numerical simulations of moving contact line problems. First, choose an affordable mesh size $h_{\min}$. Then, determine interface thickness $\epsilon \gtrsim h_{\min}$ and numerical slip $l_s \gtrsim \epsilon$ such that the results are mesh-independent. The friction coefficient β_N can be computed from l_s. Finally, adjust β_{CL} to produce the desired L_s. A larger β_{CL} is required to produce a smaller L_s.

This strategy is similar to that proposed by Yue and Feng for the phase-field method [61]. Unfortunately, we could not obtain a qualitative formula similar to that in the phase-field method to guide the choice of β_{CL} yet. This will be an important part of our future work. For now, we leave β_{CL} as a fitting parameter that needs to be calibrated based on experiments or other results, similar to that in [23]. Once calibrated, our method will be able to predict the correct contact line dynamics for a wide spectrum of contact line velocities and flow geometries, as long as the two fluids and the solid surface remain the same.

4.3.3. Comparison with experiment

In this test case, we compare our results with the experimental data on drop spreading by Zosel [62]. This also serves as an example on the usage of our computational strategy.

In the experiments, solutions of polyisobutylene in decaline with a range of concentrations were tested. It was observed that all experimental data fall onto a master curve if the dimensionless spreading radius $\frac{a}{R_0}$ is plotted against the dimensionless spreading time $\frac{t\sigma}{\mu_1 R_0}$. We choose the data points for pure polyisobutylene, which have the widest coverage on the whole master curve. Although θ_S was reported to be about 58 to 60° in the experiments, the final spreading radius, which is about $\frac{a_f}{R_0} = 1.69$, suggests a

smaller angle $\theta_S = 54^\circ$ based on (46). We thus take $\theta_S = 54^\circ$ in our simulations. The drop is initially spherical with a radius $R_0 = 0.5$ and a center at $(0, 0.48)$, such that the inner rim of the narrow-band interface just touches the wall. We set the viscosities to $\mu_1 = 1$ and $\mu_2 = 0.01$.

Following the proposed computational strategy, we first set $h_{\min} = \frac{1}{128}$ and $\epsilon = 1.5h_{\min}$. Then we pick $\beta_N = 100$ such that $l_s = \frac{\mu_1}{\beta} = 0.01$ can be resolved by $h_{\min}$ and ϵ. Finally, we tune β_{CL} to match experimental data. The spreading curves with different β_{CL} are given in Fig. 13. The curves with $\beta_{CL} = 0.5$ and $\beta_{CL} = 1$ match the experimental curve the best. For the typical drop size $R_0 \sim 1$ mm in the experiment [62], these (β_N, β_{CL}) pairs roughly correspond to an effective slip of $L_s \sim 10$ μm. Once we identify the (β_N, β_{CL}) pair for the liquid-gas-solid system, it can be used to predict the contact line dynamics under other flow conditions.

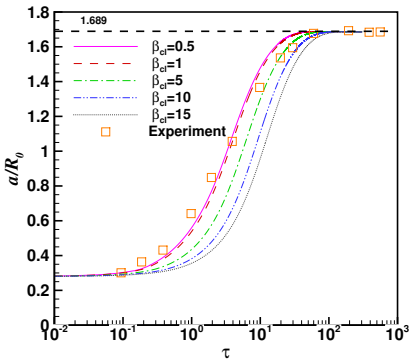

Figure 13: Comparison of drop spreading with experiment. The symbols are the experimental data for the spreading of polyisobutylene on polytetrafluoroethylene [62]. $\beta_N = 100$,$h_{\min} = 1/128$, $\epsilon = 1.5h_{\min}$, $\theta_S = 54^\circ$.

It should be noted that our numerical curves cannot match the experimental data exactly: the experimental data demonstrate a lower slope in the semi-log plot. The same trend was also observed in other numerical simulations [63, 64, 65]. This consistent discrepancy is probably because of the constant-coefficient assumptions in the contact line models. Maybe the friction coefficients β_N and β_{CL} (or the slip length) should be functions of the contact line velocity. Further investigation is beyond the scope of this paper.

4.4. Pinned drop in Poiseuille flow

We test the capability of our method in pinning contact lines by comparing with the boundary integral method [66]. A cylindrical-cap droplet, with an area of 0.5, is initially placed on a solid surface with contact angle $\theta = \pi/3$, as shown in Fig (14). The droplet is sheared by a pressure-driven flow with contact lines pinned. The capillary number is subcritical such that the drop eventually achieves a steady deformation. The flow is inertialess with $\mu_1 = \mu_2 = 1$ and $\sigma = 1$. We impose a large hysteresis window $(1^\circ, 179^\circ)$ such that the contact lines are pinned on the wall. The computational domain is a rectangle of dimensions $(0, 8) \times (0, 2)$. On the left boundary $x = 0$, we impose the inflow condition $\mathbf{u} = [u, 0]^T$ with

$$u = \frac{3}{2}\bar{V}\left(1 - (1 - y)^2\right), \tag{48}$$

where $\bar{V}$ is the average velocity in the channel. Following [66], we define the capillary number as $Ca = \frac{\mu_1 E h}{\sigma}$, where $E = 3\bar{V}$ is the shear rate at the wall (noting that the channel half height is 1) and $h = 0.4511$ is the initial height of the drop. We take $\beta_N = 100$, $\beta_{CL} = 100$, $h_{\min} = \frac{1}{64}$, and $\epsilon = 1.5h_{\min}$ in our simulations. Theoretically, since the contact lines do not move, the exact value of β_{CL} should not change the flow. However, to achieve desirable pinning performance numerically, a large enough β_{CL} needs to be used when the contact line is pinned.

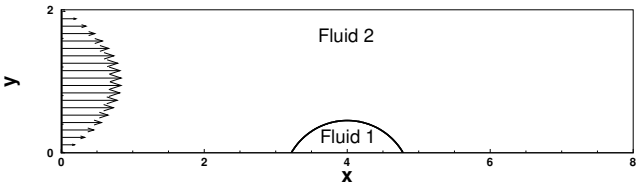

Figure 14: Schematic of a drop under shear in plane Poiseuille flow.

The steady-state drop shapes are given in Fig. 15. Our results match those of the boundary integral method almost perfectly. Since we pin the contact line through the fluid velocity, it is very difficult to achieving exact pinning due to numerical errors in computing the flow field and advecting the level-set function. Thus the contact line may shift away from its original position. At the leading (left) edge of the drop, as shown in Fig. 16(a), the contact line is blown downstream as Ca increases. This trend is probably related to the finite thickness of the numerical interface, which may cause a

large error when the interface is almost parallel to the wall, i.e., when the dynamic contact angle is close to 0° or 180°. This error is however acceptable compared to the computational mesh: the maximum displacement of the contact line is around $\frac{h_{\min}}{4}$ at $Ca = 0.15$. At the trailing (right) edge of the drop, the contact line is nicely pinned because the dynamic contact angle is close to 90°

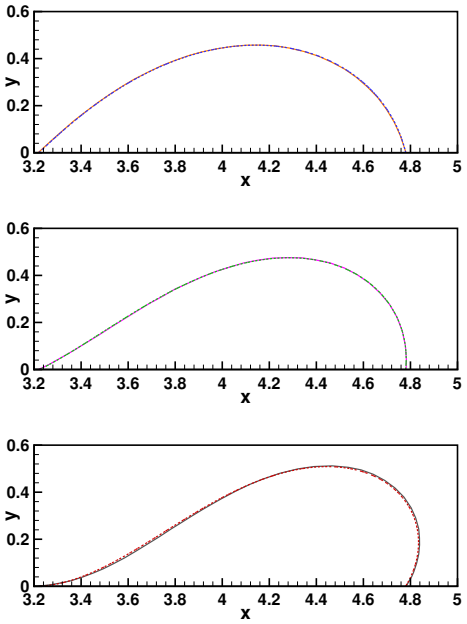

Figure 15: Comparison with the boundary-integral results of Schleizer and Bonnecaze [66]. From top to bottom, Ca=0.05, 0.10, and 0.15. The solid lines represent the boundary-integral results, while the dashed lines indicate our level-set results.

4.5. Advancing and receding contact lines in a channel

In this test case, we consider two immiscible fluids separated by two interfaces in a plane Poiseuille flow. Due to symmetry, we only compute the lower half of the channel, which is a rectangular domain $(0, 8) \times (0, 1)$, as shown in Fig. 17. The channel is long enough such that the inflow and outflow conditions are not affected by interface deformation. The two interfaces are initially vertical and located at $x = 3$ and 5, respectively. Under flow, the contact line to the left eventually recedes with respect to fluid 1 while the other contact line advances; we henceforth refer to these two contact lines as receding and advancing contact lines, respectively, even when

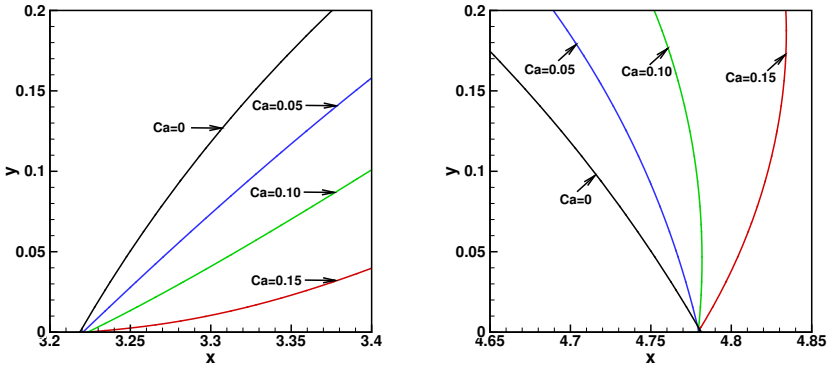

(a) Leading edge (b) Trailing edge

Figure 16: Zoomed views of the steady-state interface in the vicinity of the contact lines. $Ca = 0$ denotes the undeformed interface.

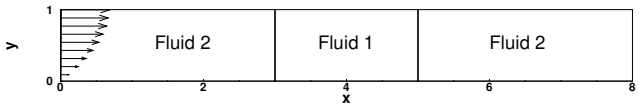

Figure 17: Schematic of advancing and receding contact lines in a channel

they are pinned. The system is inertialess and the two components have the same viscosity $\mu = 1$. The surface tension is set to $\sigma = 1$. The prescribed advancing and receding contact angles are $\theta_R = 75^\circ$ and $\theta_A = 135^\circ$, respectively. We take the following friction coefficients: $\beta_N = 100$, $\beta_{CL} = 1$ for moving contact lines, and $\beta_{CL} = 100$ for pinned contact lines. On the left boundary $x = 0$, we impose the same parabolic velocity profile as (48). We take $\bar{V} = 0.01$ such that $Ca = \frac{\mu \bar{V}}{\sigma} = 0.01$ is small enough and the deformed interfaces remain almost circular. For convenience we define a normalized time $t^* = \frac{t\bar{V}}{H}$, where $H = 1$ is the half height of the channel.

Typical interface shapes are given in Fig. 18 and the zooms at the contact line are shown in Fig. 19. The receding contact line remains pinned until about $t^* = 0.0876$ and the advancing one remains pinned until about $t^* = 0.2906$. For a circular interface with a pinned contact line, we can find the following relation between dynamic angle θ_D and normalized time t^* based on mass conservation [38]: $t^* = \frac{1}{2}\frac{H}{V}\left(\frac{\delta}{\sin^2\delta} - \cot\delta\right)$, where $\delta = |\frac{\pi}{2} - \theta_D|$. This gives $t^* = 0.0881$ for the receding contact line to achieve $\theta_D = 75^\circ$ and $t^* = 0.2854$ for the advancing contact line to achieve $\theta_D = 135^\circ$. Our

numerical depinning times agree with these theoretical predictions very well.

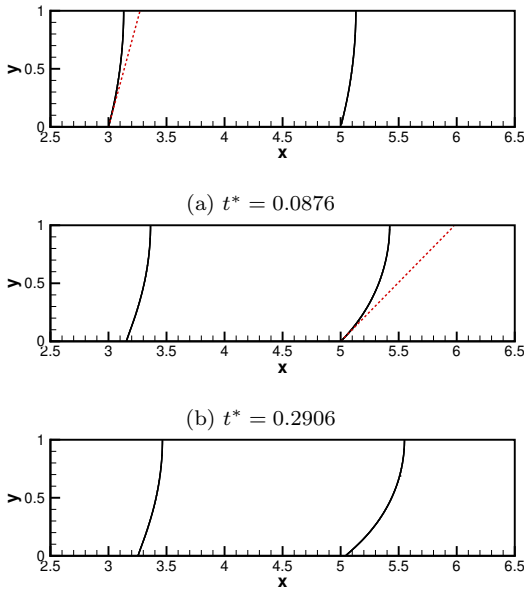

(a) $t^* = 0.0876$

(b) $t^* = 0.2906$

(c) $t^* = 0.3926$

Figure 18: Shapes of advancing and receding interfaces in a channel. The red dotted lines correspond to the receding angle $\theta_R = 75^\circ$ and the advancing angle $\theta_A = 135^\circ$, respectively.

4.6. Sliding drop

This test case is adapted from [35]. We consider the deformation of a drop on a wall which is slowly inclined, as shown in Fig. 20. The drop is initially semicircular with radius $R_0 = 0.5$, and the computational domain is a rectangle of 5×1. The finest mesh is set to $h_{\min} = \frac{1}{128}$. We choose the following fluid properties: $\rho_1 = 1$, $\rho_2 = 0.01$, $\mu_1 = 1$, $\mu_2 = 0.1$, and $\sigma = 1$. Since $\rho_2 \ll \rho_1$, we define the Bond number as $Bo = \rho_1 g R_0^2/\sigma$, according to which the magnitude of gravitational acceleration g is adjusted to achieve different Bo. The wall is initially horizontal and slowly inclined until the drop starts to slide. Each inclination angle α is maintained for a period of the greater of the inertia-capillary time $\sqrt{\rho_1 R_0^3/\sigma}$ and the visco-capillary time $\mu_1 R_0/\sigma$, which is 0.5 for our chosen parameters, to allow enough time for the drop to deform. The increment of slop angle varies depending on whether the inclination angle is near critical. In the simulations, instead of rotating the computational domain, we rotate the gravitational acceleration

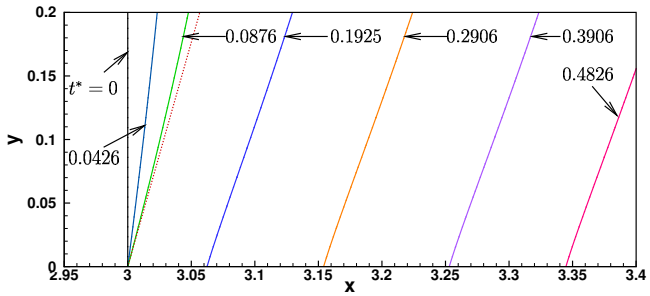

(a) Receding interface

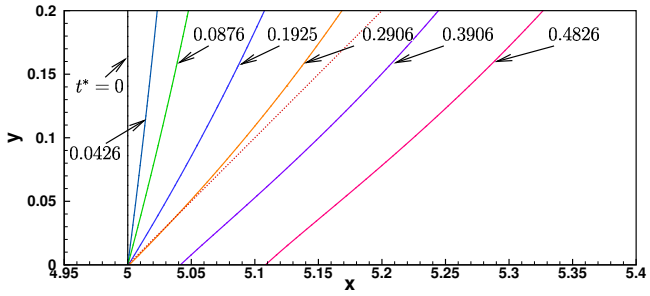

(b) Advancing interface

Figure 19: Evolution of the interfaces in the vicinity of the contact lines.

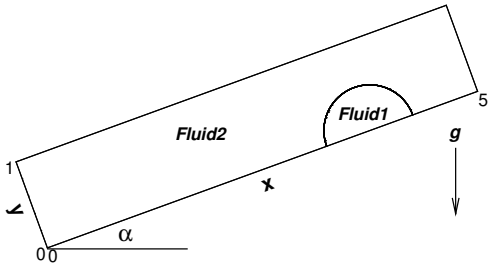

Figure 20: Schematic of a drop on an inclined wall.

$\mathbf{g} = -g(\sin\alpha, \cos\alpha)$. For the contact line, we take $\beta_N = 100$, $\beta_{CL} = 1$ at the moving contact line, and $\beta_{CL} = 100$ at the pinned contact line.

Theoretically, based on a force balance along the wall, one can derive the critical inclination angle α_c when the drop starts to slide [67, 68]:

$$\frac{1}{2}\pi R^2 \rho_1 g \sin\alpha_c = \sigma(\cos\theta_R - \cos\theta_A), \tag{49}$$

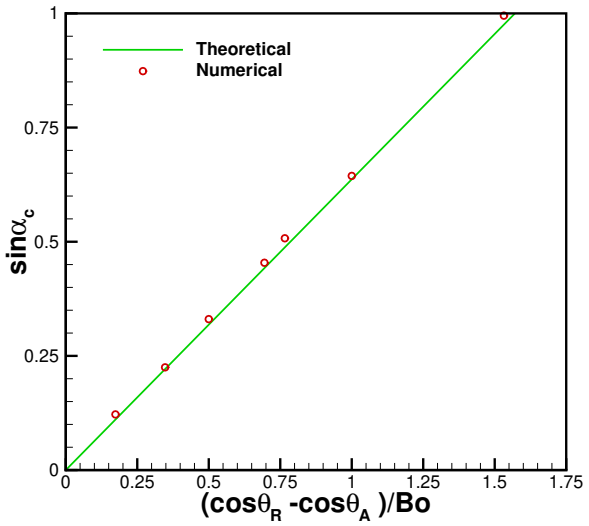

Figure 21: Critical inclination angle α_c versus $(\cos\theta_R - \cos\theta_A)/\mathrm{Bo}$.

which can be rewritten as

$$\sin\alpha_c = \frac{2}{\pi \mathrm{Bo}} \left(\cos\theta_R - \cos\theta_A\right). \tag{50}$$

By choosing different hysteresis angles and Bond numbers, we can compute the corresponding critical inclination angles α_c and compare against the theoretical relation (50). Here, we test Bo = 0.5, 1.0 and 2.0 with different hysteresis angles $(\theta_R, \theta_A) = (80^\circ, 100^\circ), (60^\circ, 120^\circ)$, and $(40^\circ, 140^\circ)$, which are the same as in [35]. The critical inclination angles are summarized in Fig. 21, which indicates a very good agreement with the theoretical relation (50). Quantitatively, the agreement is better than that obtained by the volume-of-fluid method in [35]. In terms of computational mesh, our finest mesh size is slightly smaller, but the total number of cells, typically around 2000, is much less than the 500×100 uniform mesh in [35].

The critical drop shapes are displayed in Fig. 22. For small Bond numbers, when the hysteresis is sufficiently large, the drop is pinned on the wall even when the inclination angle achieves 90°. For example, at $Bo = 0.5$, the drops are pinned on the wall with identical shapes for $(\theta_R, \theta_A) = (60^\circ, 120^\circ)$ and $(40^\circ, 140^\circ)$. In these two cases, α_c does not exist.

Drop shape evolutions for selected parameters are given in Fig. 23. Each curve denotes the interface obtained with the inclination angle α being fixed

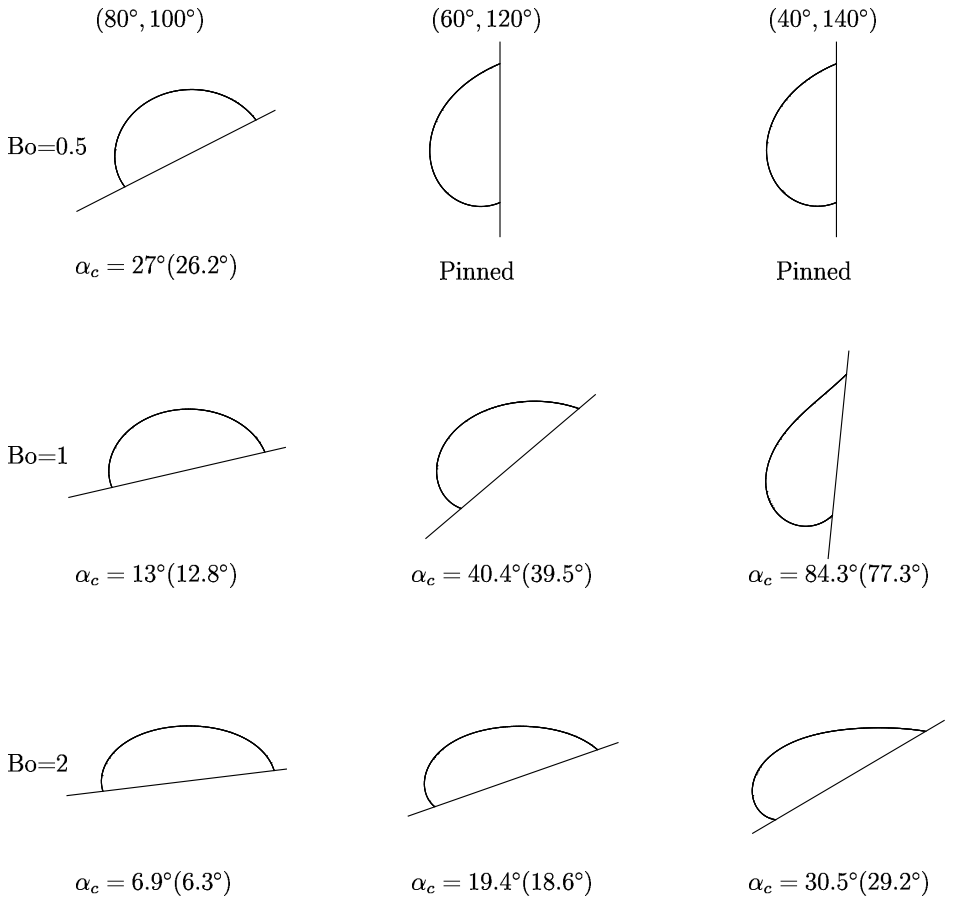

Figure 22: Drop shapes at critical inclination angles. Bo is fixed in each row and (θ_R, θ_A) is fixed in each column. The theoretical values of α_c are given in the parentheses.

for a time span of 0.5. It can be viewed approximately as the steady drop shape for the given α. In (a), gravity is dominant and θ_A is close to the initial contact angle of 90°. At $\alpha = 0°$, the drop spreads due to gravity. As α increases, the dynamic contact angle at the advancing contact line (left) increases and the one at the receding contact line (right) decreases. The advancing contact line moves first with the receding one pinned at $\alpha = 3°$. At $\alpha = 6.9°$, the receding contact line starts to move at a very low speed and this angle is recorded as the critical inclination angle. In (b), the hysteresis window is increased to $(60°, 120°)$. θ_A is big enough to inhibit the initial drop spreading at $\alpha = 0°$: the drop flattens under gravity, but the contact lines remain pinned. The later dynamics is similar to that in (a). At a

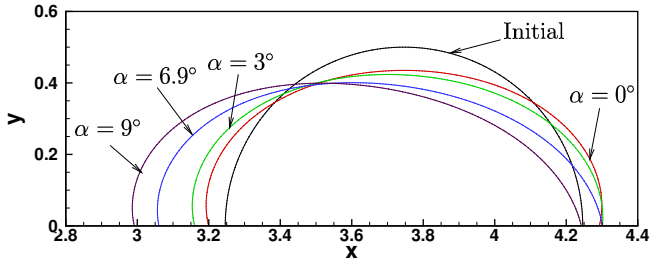

(a) $Bo = 2$, $\theta_A = 100°$, $\theta_R = 80°$.

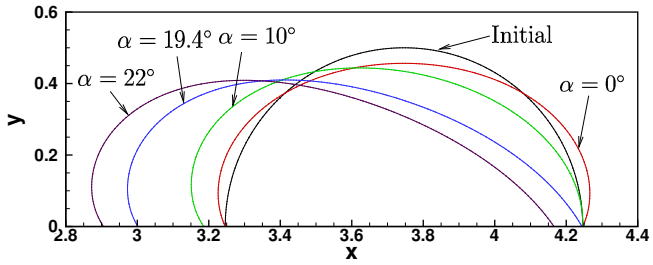

(b) $Bo = 2$, $\theta_A = 120°$, $\theta_R = 60°$.

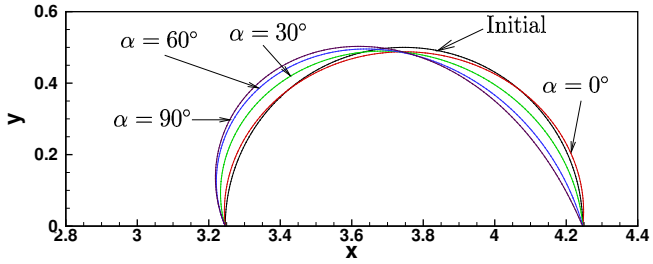

(c) $Bo = 0.5$, $\theta_A = 120°$, $\theta_R = 60°$.

Figure 23: Evolutions of drop shapes.

sufficiently small Bo, gravity is insufficient to overcome the contact angle hysteresis, as shown in (c). As a result, the drop deforms with contact lines pinned.

5. Concluding remarks

We have developed a level-set method, where the level-set function is reinitialized by an interface-preserving method that we previously developed. The flow equations are solved by a continuous finite element method while the level-set equation is solved by a discontinuous Galerkin method on an adaptive quadrilateral mesh. After a careful validation against the Cox theory, we come up with a computational strategy for practical contact line simulations. Furthermore, our method can be easily modified to accommodate contact angle hysteresis. The main results can be summarized as follows.

(i) Reasonable accuracy can be achieved as long as the mesh size $h_{\min}$ is able to resolve the interfacial thickness ϵ and the numerical slip $l_s = \frac{\mu}{\beta_N}$: $h_{\min} \lesssim \epsilon \lesssim l_s$. For a sharp-interface method that does not use the continuum surface force method to apply surface tension, we expect this criterion to reduce to $h_{\min} \lesssim l_s$.

(ii) In addition to β_N, the contact line friction β_{CL} also affects the effective slip length. In particular, a single slip length in the Cox theory can be reproduced by different combinations of (β_N, β_{CL}). In practical computations, we suggest to prescribe β_N based on the mesh convergence requirement and then use β_{CL} as the only fitting parameter to achieve desired slip. By using this strategy, we have obtained a reasonable agreement with the drop spreading experiment. Since our method does not rely on external models to impose the contact angle condition, it is easy to implement numerically.

(iii) In our method, the dynamic contact angle can be readily obtained from the level-set function, based on which we can determine whether the contact line is pinned, advancing, or receding. Meanwhile, the weak form for the pinned contact line only differs a little from that for the moving contact line. All these properties make it easy to incorporate contact angle hysteresis. More importantly, our method demonstrates very good accuracy in capturing hysteresis.

Although this work focuses on the level-set method, we expect the computational strategy and hysteresis model to be applicable to a wide range of numerical methods with the generalized Navier slip condition. All the simulations are in 2D, but the formulations are ready for 3D and the development of an efficient 3D flow solver is currently ongoing.

Acknowledgements

This work was supported by the National Science Foundation (Grant DMS-1522604). The authors thank Tiezheng Qian and Weiqing Ren for stimulating discussions. We also acknowledge Advanced Research Computing at Virginia Tech for providing computational resources and technical support that have contributed to the results in this paper.

References

[1] M.-Y. Zhou and P. Sheng, Dynamics of immiscible-fluid displacement in a capillary tube *Phys. Rev. Lett.*, vol. 64, pp. 882–885, 1990.

[2] D. Jacqmin, Contact-line dynamics of a diffuse fluid interface *J. Fluid Mech.*, vol. 402, pp. 57–88, 2000.

[3] S. Zahedi, K. Gustavsson, and G. Kreiss, A conservative level set method for contact line dynamics *J. Comput. Phys.*, vol. 228, no. 17, pp. 6361 – 6375, 2009.

[4] M. Sbragalia, K. Sugiyama, and L. Biferale, Wetting failure and contact line dynamics in a couette flow *J. Fluid Mech.*, vol. 614, pp. 471–493, 2008.

[5] T. Qian, X.-P. Wang, and P. Sheng, Molecular scale contact line hydrodynamics of immiscible flows *Phys. Rev. E*, vol. 68, p. 016306, 2003.

[6] W. Ren and W. E, Boundary conditions for the moving contact line problem *Phys. Fluids*, vol. 19, p. 022101, 2007.

[7] Y. Sui, H. Ding, and P. D. Spelt, Numerical simulations of flows with moving contact lines *Annu. Rev. Fluid Mech.*, vol. 46, no. 1, pp. 97–119, 2014.

[8] T. Qian, X.-P. Wang, and P. Sheng, A variational approach to moving contact line hydrodynamics *J. Fluid Mech.*, vol. 564, pp. 333–360, 2006.

[9] W. Ren and W. E, Derivation of continuum models for the moving contact line problem based on thermodynamic principles *Commun. Math. Sci.*, vol. 9, pp. 597–606, 2011.

[10] X. Xu, Y. Di, and H. Yu, Sharp-interface limits of a phase-field model with a generalized navier slip boundary condition for moving contact lines *J. Fluid Mech.*, vol. 849, p. 805–833, 2018.

[11] Y. Di and X.-P. Wang, Precursor simulations in spreading using a multi-mesh adaptive finite element method *J. Comput. Phys.*, vol. 228, no. 5, pp. 1380–1390, 2009.

[12] Q. Zhang, T.-Z. Qian, and X.-P. Wang, Phase field simulation of a droplet impacting a solid surface *Phys. Fluids*, vol. 28, no. 2, p. 022103, 2016.

[13] F. Bai, X. He, X. Yang, R. Zhou, and C. Wang, Three dimensional phase-field investigation of droplet formation in microfluidic flow focusing devices with experimental validation *Int. J. Multiph. Flow*, vol. 93, pp. 130–141, 2017.

[14] L. Luo, X.-P. Wang, and X.-C. Cai, An efficient finite element method for simulation of droplet spreading on a topologically rough surface *J. Comput. Phys.*, vol. 349, pp. 233 – 252, 2017.

[15] T. Omori and T. Kajishima, Apparent and microscopic dynamic contact angles in confined flows *Phys. Fluids*, vol. 29, no. 11, p. 112107, 2017.

[16] J.-F. Gerbeau and T. Lelièvre, Generalized Navier boundary condition and geometric conservation law for surface tension *Comput. Methods Appl. Mech. Eng.*, vol. 198, no. 5, pp. 644 – 656, 2009.

[17] Z. Li, M.-C. Lai, G. He, and H. Zhao, An augmented method for free boundary problems with moving contact lines *Comput. & Fluids*, vol. 39, no. 6, pp. 1033–1040, 2010.

[18] W. Ren and W. E, Contact line dynamics on heterogeneous surfaces *Phys. Fluids*, vol. 23, p. 072103, 2011.

[19] J.-J. Xu and W. Ren, A level-set method for two-phase flows with moving contact line and insoluble surfactant *J. Comput. Phys.*, vol. 263, pp. 71 – 90, 2014.

[20] Z. Zhang and W. Ren, Simulation of moving contact lines in two-phase polymeric fluids *Comput. & Math. with Appl.*, vol. 72, no. 4, pp. 1002 – 1012, 2016.

[21] Y. Yamamoto, T. Ito, T. Wakimoto, and K. Katoh, Numerical simulations of spontaneous capillary rises with very low capillary numbers using a front-tracking method combined with generalized navier boundary condition *Int. J. Multiph. Flow*, vol. 51, pp. 22 – 32, 2013.

[22] A. M. Boelens and J. J. de Pablo, Generalised navier boundary condition for a volume of fluid approach using a finite-volume method *Phys. Fluids*, vol. 31, no. 2, p. 021203, 2019.

[23] H. S. H. Mohand, H. Hoang, G. Galliero, and D. Legendre, On the use of a friction model in a volume of fluid solver for the simulation of dynamic contact lines *J. Comput. Phys.*, vol. 393, pp. 29 – 45, 2019.

[24] M. Fricke, M. Köhne, and D. Bothe, A kinematic evolution equation for the dynamic contact angle and some consequences *Phys. D: Nonlinear Phenom.*, vol. 394, pp. 26 – 43, 2019.

[25] M. Fricke, T. Marić, and D. Bothe, Contact line advection using the level set method *PAMM*, vol. 19, no. 1, p. e201900476, 2019.

[26] S. Afkhami, S. Zaleski, and M. Bussmann, A mesh-dependent model for applying dynamic contact angles to vof simulations *J. Comput. Phys.*, vol. 228, no. 15, pp. 5370–5389, 2009.

[27] Y. Sui and P. D. Spelt, An efficient computational model for macroscale simulations of moving contact lines *J. Comput. Phys.*, vol. 242, pp. 37 – 52, 2013.

[28] D. Legendre and M. Maglio, Comparison between numerical models for the simulation of moving contact lines *Comput. & Fluids*, vol. 113, pp. 2 – 13, 2015. Small scale simulation of multiphase flows.

[29] S. Afkhami, J. Buongiorno, A. Guion, S. Popinet, Y. Saade, R. Scardovelli, and S. Zaleski, Transition in a numerical model of contact line dynamics and forced dewetting *J. Comput. Phys.*, vol. 374, pp. 1061 – 1093, 2018.

[30] O. V. Voinov, Hydrodynamics of wetting *J. Fluid Mech.*, vol. 11, no. 5, pp. 714–721, 1976. Translated from Izvestiya Akademii Nauk SSSR, Mekhanika Zhidkosti i Gaza, No. 5, pp. 76–84, September–October, 1976.

[31] R. G. Cox, The dynamics of the spreading of liquids on a solid surface. Part 1. Viscous flow *J. Fluid Mech.*, vol. 168, pp. 169–194, 1986.

[32] Y. Yamamoto, K. Tokieda, T. Wakimoto, T. Ito, and K. Katoh, Modeling of the dynamic wetting behavior in a capillary tube considering the macroscopic-microscopic contact angle relation and generalized navier boundary condition *Int. J. Multiph. Flow*, vol. 59, pp. 106 – 112, 2014.

[33] P. D. Spelt, A level-set approach for simulations of flows with multiple moving contact lines with hysteresis *J. Comput. Phys.*, vol. 207, no. 2, pp. 389 – 404, 2005.

[34] H. Ding and P. D. M. Spelt, Onset of motion of a three-dimensional droplet on a wall in shear flow at moderate reynolds numbers *J. Fluid Mech.*, vol. 599, pp. 341–362, 2008.

[35] J.-B. Dupont and D. Legendre, Numerical simulation of static and sliding drop with contact angle hysteresis *J. Comput. Phys.*, vol. 229, no. 7, pp. 2453 – 2478, 2010.

[36] L. Wang, H.-B. Huang, and X.-Y. Lu, Scheme for contact angle and its hysteresis in a multiphase lattice boltzmann method *Phys. Rev. E*, vol. 87, p. 013301, Jan 2013.

[37] S. Shin, J. Chergui, and D. Juric, Direct simulation of multiphase flows with modeling of dynamic interface contact angle *Theor. Comput. Fluid Dyn.*, vol. 32, pp. 655–687, Oct 2018.

[38] P. Yue, Thermodynamically consistent phase-field modelling of contact angle hysteresis *J. Fluid Mech.*, 2020. accepted.

[39] S. Osher and J. Sethian, Fronts propagating with curvature dependent speed: algorithms based on hamilton-jacobi formulations *J. Comput. Phys.*, vol. 79, pp. 12–49, 1988.

[40] M. Sussman, P. Smereka, and S. Osher, A level set approach for computing solutions to incompressible two-phase flow *J. Comput. Phys.*, vol. 114, pp. 146–159, 1994.

[41] B. Lafaurie, C. Nardone, R. Scardovelli, S. Zaleski, and G. Zanetti, Modelling merging and fragmentation in multiphase flows with surfer *J. Comput. Phys.*, vol. 113, no. 1, pp. 134 – 147, 1994.

[42] T. D. Blake, The physics of moving wetting lines *J. Colloid Interface Sci.*, vol. 299, pp. 1–13, 2006.

[43] J. Zhang and P. Yue, A high-order and interface-preserving discontinuous galerkin method for level-set reinitialization *J. Comput. Phys.*, vol. 378, pp. 634–664, 2019.

[44] C. Hu and C.-W. Shu, A discontinuous galerkin finite element method for Hamilton-Jacobi equations *SIAM J. Sci. Comput.*, vol. 21, pp. 666–690, 1999.

[45] S. Xu and W. Ren, Reinitialization of the level-set function in 3d simulation of moving contact lines *Commun. Comput. Phys.*, vol. 20, no. 5, pp. 1163–1182, 2016.

[46] W. Bangerth, R. Hartmann, and G. Kanschat, deal.II – a general purpose object oriented finite element library *ACM Trans. Math. Softw.*, vol. 33, no. 4, pp. 24/1–24/27, 2007.

[47] G. Alzetta, D. Arndt, W. Bangerth, V. Boddu, B. Brands, D. Davydov, R. Gassmoeller, T. Heister, L. Heltai, K. Kormann, M. Kronbichler, M. Maier, J.-P. Pelteret, B. Turcksin, and D. Wells, The `deal.II` library, version 9.0 *J. Numer. Math.*, vol. 26, no. 4, pp. 173–183, 2018.

[48] S. Gottlieb and C.-W. Shu, Total variation diminishing runge-kutta schemes *Math. Comp.*, vol. 67, pp. 73–85, 1998.

[49] T. A. Davis, Algorithm 832: Umfpack v4.3—an unsymmetric-pattern multifrontal method *ACM Trans. Math. Softw.*, vol. 30, pp. 196–199, June 2004.

[50] J. Hnat and J. Buckmaster, Spherical cap bubbles and skirt formation *Phys. Fluids*, vol. 19, no. 2, pp. 182–194, 1976.

[51] G. Ryskin and L. Leal, Numerical solution of free-boundary problems in fluid mechanics. part 2. buoyancy-driven motion of a gas bubble through a quiescent liquid *J. Fluid Mech.*, vol. 148, pp. 19–35, 1984.

[52] M. Sussman and P. Smereka, Axisymmetric free boundary problems *J. Fluid Mech.*, vol. 341, pp. 269–294, 1997.

[53] D. Gueyffier, J. Li, A. Nadim, R. Scardovelli, and S. Zaleski, Volume-of-fluid interface tracking with smoothed surface stress methods for three-dimensional flows *J. Comput. Phys.*, vol. 152, no. 2, pp. 423 – 456, 1999.

[54] M. Ohta, T. Imura, Y. Yoshida, and M. Sussman, A computational study of the effect of initial bubble conditions on the motion of a gas bubble rising in viscous liquids *Int. J. Multiph. Flow*, vol. 31, no. 2, pp. 223–237, 2005.

[55] P. Yue, J. J. Feng, C. A. Bertelo, and H. H. Hu, An arbitrary lagrangian–eulerian method for simulating bubble growth in polymer foaming *J. Comput. Phys.*, vol. 226, no. 2, pp. 2229–2249, 2007.

[56] M. Renardy, Y. Renardy, and J. Li, Numerical simulation of moving contact line problems using a volume-of-fluid method *J. Comput. Phys.*, vol. 171, no. 1, pp. 243–263, 2001.

[57] P. Yue, C. Zhou, and J. J. Feng, Sharp-interface limit of the Cahn-Hilliard model for moving contact lines *J. Fluid Mech.*, vol. 645, pp. 279–294, 2010.

[58] R. L. Hoffman, A study of the advancing interface *J. Colloid Interface Sci.*, vol. 50, pp. 228–241, 1975.

[59] T. Blake and J. Haynes, Kinetics of liquid/liquid displacement *J. Colloid Interface Sci.*, vol. 30, no. 3, pp. 421 – 423, 1969.

[60] M. Wörner, X. Cai, H. Alla, and P. Yue, A semi-analytical method to estimate the effective slip length of spreading spherical-cap shaped droplets using cox theory *Fluid Dyn. Res.*, vol. 50, no. 3, p. 035501, 2018.

[61] P. Yue and J. J. Feng, Wall energy relaxation in the Cahn-Hilliard model for moving contact lines *Phys. Fluids*, vol. 23, p. 012106, 2011.

[62] A. Zosel, Studies of the wetting kinetics of liquid drops on solid surfaces *Colloid Polym. Sci.*, vol. 271, no. 7, pp. 680–687, 1993.

[63] V. V. Khatavkar, P. D. Anderson, and H. E. H. Meijer, Capillary spreading of a droplet in the partially wetting regime using a diffuse-interface model *J. Fluid Mech.*, vol. 572, pp. 367–387, 2007.

[64] X. Cai, H. Marschall, M. Wörner, and O. Deutschmann, Numerical simulation of wetting phenomena with a phase-field method using OpenFOAM *Chem. Eng. & Technol.*, vol. 38, no. 11, pp. 1985–1992, 2015.

[65] J. Luo, X. Hu, and N. A. Adams, Curvature boundary condition for a moving contact line *J. Comput. Phys.*, vol. 310, pp. 329–341, 2016.

[66] A. D. Schleizer and R. T. Bonnecaze, Displacement of a two-dimensional immiscible droplet adhering to a wall in shear and pressure-driven flows *J. Fluid Mech.*, vol. 383, p. 29–54, 1999.

[67] C. Furmidge, Studies at phase interfaces. i. the sliding of liquid drops on solid surfaces and a theory for spray retention *J. Colloid Sci.*, vol. 17, no. 4, pp. 309 – 324, 1962.

[68] E. B. Dussan V. and R. T.-P. Chow, On the ability of drops or bubbles to stick to non-horizontal surfaces of solids *J. Fluid Mech.*, vol. 137, pp. 1–29, 1983.